Fe(III) uptake by calcium silicate hydrates

A. Mancini[1,3]*, E. Wieland[1], G. Geng[1], R. Dähn[1], J. Skibsted[2], B. Wehrli[3], B. Lothenbach[4,5]

[1] Paul Scherrer Institut, Laboratory for Waste Management, 5232 Villigen PSI, Switzerland

[2] Aarhus University, Department of Chemistry and iNANO, Laboratory for Solid-State NMR Spectroscopy of Inorganic Materials, Langelandsgade 140, DK-8000 Aarhus-C, Denmark

[3] ETH Zurich, Institute of Biogeochemistry and Pollutant Dynamics, 8092 Zurich, Switzerland

[4] Empa, Laboratory for Concrete & Construction Chemistry, 8600 Dübendorf, Switzerland

[5] NTNU, Department of Structural Engineering, Trondheim, Norway

Prepared for publication in *Applied Geochemistry*

*corresponding author:

Paul Scherrer Institut

Laboratory for Waste Management

5232 Villigen PSI

Switzerland

Tel.: +41 56 310 2291

Fax: +41 56 310 3565

E-Mail address: andrea.mancini@psi.ch

Key words: ferric iron, calcium silicate hydrates, X-ray absorption spectroscopy, sorption

Abstract

Wet chemistry and spectroscopic investigations were conducted to study Fe(III) uptake by calcium-silicate-hydrate (C-S-H) at different Ca/Si ratios. Wet chemistry experiments were carried out by using a ^{55}Fe radiotracer while ^{29}Si NMR and XAS spectroscopy were performed on C-S-H phases loaded with different Fe(III) concentrations. Sorption kinetics experiments indicates that equilibrium was attained within 30 days. Over the studied concentration range, Fe(III) sorption was linear, irrespective of the difference in pH of the suspension and the Ca/Si of C-S-H. In addition, Fe(III) sorption on C-S-H phases was significantly stronger than Al(III) sorption. The total Fe(III) uptake by C-S-H phases, however, was limited by the lower solubility of $Fe(OH)_3$ compared to $Al(OH)_3$; up to 1 mol Fe/kg C-S-H (molar Fe(III)/ Si ≈ 0.001) could be taken up. ^{29}Si NMR and EXAFS data suggest Fe(III) uptake in octahedral coordination into the interlayer of the C-S-H phases with Ca/Si ratios 1.2 and 1.5. However, such an uptake mechanism appears unlikely in the case of the C-S-H phase with Ca/Si 0.8 because structural parameters of Fe(III) deduced from EXAFS are different.

1 Introduction

Understanding the mechanisms of iron interaction with cementitious materials is of utmost importance for predicting the service life and design of reinforced concrete structures. Accelerated corrosion of iron results in the precipitation of corrosion products at the interface with cement paste, which leads to corrosion-induced damage by expansive cracking of the concrete cover (Bertolini et al., 2013). Interaction of iron with cementitious materials could also have an impact on the long-term performance of the engineered barriers in cement-based repositories for low and intermediate level waste (L/ILW). Safety assessments consider that cementitious materials significantly retard the release of hazardous radionuclides into the surrounding environment (Chapman and McCombie, 2003). It is anticipated that the barrier effect of cementitious materials against radionuclide release will be effective over tens of thousands of years. Over this long period of time, corrosion-induced long-term interaction of ferric and ferrous iron with cement phases could lead to phase changes in the cement matrix and thereby severely reduce the barrier effect.

In the area of research related to the safe disposal of radioactive waste, reliable predictions of materials behavior for such long periods of time are increasingly based on appropriate modelling approaches involving chemical reactions and transport processes in connection with the temporal evolution of the chemical conditions in the cementitious near field of a L/ILW repository (e.g. Huang et al., 2018). In this context, corrosion science faces a new challenge that is allowing reliable prediction of natural corrosion processes over the very long time of concern for a repository for radioactive waste, which was set to 10^5 years in the Swiss disposal concept for L/ILW. It is worth noting that a combination of chemical reactions, i.e. the oxidation of ferrous iron, and diffusive transport of the ion has recently been proposed to improve predictions of the progress of natural corrosion processes with time (Stefanoni et al., 2018). Implementation of chemical processes in numerical codes for reactive transport further requires that the relevant chemical species can be expressed in terms of their thermodynamic properties. In the case of cementitious systems the progress made in the development of thermodynamic models and determination of the necessary thermodynamic data (Lothenbach and Winnefeld, 2006; Lothenbach et al., 2011; Lothenbach et al., 2019) allows, nowadays, to accurately predict the mineral compositions of cement pastes and chemical compositions of the pore solutions of cement pastes in the course of the hydration process. This is possible for a large variety of cement types and for a wide range of conditions, such as variations in the initial compositions of the cements, changes in temperature, and the effect of external parameters, as for example the ingress of porewater from geological formations that promote cement alteration (e.g. Damidot et al., 2011; Kosakowski and Berner 2013; Lothenbach et al., 2010; Lothenbach et al., 2011) . Nevertheless, the interaction of iron corrosion products with cementitious materials, in particular in anoxic (i.e. reducing) conditions, are presently not adequately modelled due to the lack of thermodynamic data for Fe interaction with calcium silicate hydrate (C-S-H) phases. The present study aims to improve the current situation by providing a mechanistic understanding of Fe(III) uptake by C-S-H for future thermodynamic modelling of interaction processes during the course of iron/steel corrosion in concrete structures. Note that the uptake of Fe(II) by C-S-H phases is currently being investigated in a parallel study (Mancini et al., 2019).

The sorption potential of metal cations of cement paste is mainly determined by C-S-H phases, which is the most abundant component of cement paste. C-S-H phases produced by

cement hydration are nearly amorphous, but they are subjected to high recrystallization rates (Mandaliev et al., 2010a). Their structural order can be described by a defective tobermorite structure, i.e. calcium oxide layers bonded to dreierketten silica chains on both sides (Allen et al., 2007; Merlino et al., 2001; Richardson, 2004; Taylor, 1997). The layered structure of these silica chains and Ca-O layers is intercalated by an interlayer space, where increasing amount of Ca is hosted when Ca/Si increases (Geng et al., 2017; Lothenbach and Nonat, 2015; Renaudin et al., 2009b;). The interlayer was found to also expose hosting sites for radionuclide uptake. The uptake potential of C-S-H phases has been studied for several radionuclides, such as Zn(II) (Ziegler et al., 2001), U(VI) (Harfouche et al., 2006; Tits et al., 2011), Eu(III) (Pointeau et al., 2001; Schlegel et al., 2004), Sr(II) (Tits et al., 2006a), Ra(II) (Lange et al., 2018; Olmeda et al., 2019; Tits et al., 2006b), Np(IV) (Gaona et al., 2011; Tits et al., 2014), and Nd(III) (Mandaliev et al., 2010a; Mandaliev et al., 2010b).

In addition to heavy metals, the incorporation of Al(III) in C-S-H phases has been observed, forming the so-called C-A-S-H phases (Andersen et al., 2003; L'Hôpital et al., 2015; L'Hôpital et al., 2016a; L'Hôpital et al., 2016b; Myers et al., 2015; Richardson et al., 1993). Al(III) is incorporated in different coordination environments in C-S-H phases depending on the Ca/Si and Al/Si ratios (L'Hôpital et al., 2016b). For example, at low Ca/Si ratio, Al(III) in tetrahedral coordination replaces Si(IV) at the bridging position of the dreierketten silica chains while at high Ca/Si ratio Al(III) in octahedral coordination competes with other cations for uptake into the interlayer of C-S-H.

In strongly alkaline solution, Fe(III) is known to have a tetrahedral coordination geometry (Sipos et al., 2008). At the same conditions, in complex salts, Fe(III) is found to be bound preferentially in octahedral coordination (Sipos et al., 2008). Ferric iron is known to replace Al(III) in Al(III)-bearing cement phases, such as Fe-ettringite, Fe-monosulphate, Fe-hemicarbonate, and Fe-monocarbonate (Dilnesa et al., 2011; Dilnesa et al., 2012; Möschner et al., 2008; Möschner et al., 2009). Furthermore, Fe/Al siliceous hydrogarnet was identified as the thermodynamically stable Fe(III)-bearing phase in ordinary Portland cement (Dilnesa et al., 2014a, 2014b; Vespa et al., 2015). Fe(III) uptake by C-S-H phase is still poorly understood while evidence for Fe(III)-C-S-H interactions exists. Labhasetwar and co-authors (1991) postulated that Fe(III) is taken up into the interlayer space of C-S-H phases at low Ca/Si ratio coinciding with Ca(II) release. On the basis of results from Mössbauer spectroscopy the authors further postulated that Fe(III) is present in octahedral

coordination in the interlayer. Also Faucon et al. (1996) reported that Ca(II) in C-S-H is replaced by Fe(III) during cement leaching.

In this study, Fe(III) uptake by C-S-H phases was investigated by wet chemistry experiments, ^{29}Si NMR, and X-ray absorption spectroscopy (XAS). Kinetics of the uptake process and sorption isotherms were determined. Moreover, the pH dependence of the Fe(III) speciation and its consequences on the uptake process as well as the effect of the Ca/Si ratio on the uptake process were studied. A mechanistic model for the uptake process is proposed and a comparison is made between the structural models for Fe(III) and Al(III) uptake by C-S-H phases. In this paper Fe always refers to Fe(III), unless stated otherwise.

2 Material and methods

2.1 Materials

2.1.1 General

Throughout this study the solutions were prepared using "pro analysis" (analytical-grade) chemicals. Deionized, de-carbonated water (Milli-Q water; 18.2 MΩ·cm^{-1}) generated by a Milli-Q Gradient A10 purification system (Millipore Billerca, USA) was used for the preparation of solutions and for sample dilution. The pollyallomere centrifuge tubes (Beckman Instruments Inc.) used for the wet chemistry experiments were washed, left overnight in a solution of 0.1 M HCl, and thoroughly rinsed with deionized water. All wet chemistry experiments were carried out in glove boxes under a N_2 atmosphere (O_2, CO_2 < 0.1 ppm)

2.1.2 Titanium dioxide

A titanium dioxide (TiO_2) suspension was prepared according to a procedure by Tits et al. (2014). The material (Aeroxide P25, Evonik Industries AG, Germany) is a mixture of 86% anatase and 14% rutile. For the sorption experiments, the pH of the suspensions was adjusted with 1.0 M NaOH solution. The pH had to be adjusted several times over a period of few days to compensate for the deprotonation reactions on the TiO_2 surface.

2.1.3 Synthesis and characterization of C-S-H phases

C-S-H phases were prepared by mixing CaO (calcium oxide) and SiO_2 (silica fume Aerosil 300, Evonik Industries AG, Germany) in different proportions according to the target Ca/Si ratios (i.e. 0.8, 1.2, 1.5) and using the "direct reaction" method (Atkins et al., 1992; Tits et al., 2006a). Hereafter they will be denoted as C-S-H 0.8, C-S-H 1.2, and C-S-H 1.5, respectively. CaO was prepared by decomposing $CaCO_3$ (Merck, Germany) at 1000°C until a constant weight was achieved. Deionized, ultrapure Milli-Q water was boiled and purged with nitrogen for 2 hours. Stoichiometric amounts of CaO and SiO_2 were mixed to reach a final solid-to-liquid ratios (based upon the dry mass CaO + SiO_2) of 5 g/L for the sorption experiments. NaOH was used to adjust the pH of the suspensions if necessary. The suspensions were stored in closed polyethylene (PE)-flasks and equilibrated on an end-over-end shaker for one month in the glove box with N_2 atmosphere prior to use. After one month, an aliquot of each suspension was sampled for the characterization of the solid phase, where the solid and liquid phases were separated by centrifugation (1 h, 95,000 g). The supernatant solution was filtered through a 0.22 µm nylon filter. The solids were dried in equilibrium with 8% NaOH solution in an airtight box placed in the glove box with N_2 atmosphere and subsequently analysed by X-ray diffraction (XRD) and thermogravimetric analysis (TGA).

2.2 Sorption experiments

Batch sorption experiments were carried out with Fe on the synthesised C-S-H phases and TiO_2 to determine the partitioning of Fe between solid and liquid phase. Fe partitioning was determined as a function of equilibration time (kinetics) and Fe loadings (sorption isotherms). Radiotracer experiments with ^{55}Fe were carried by diluting small quantities of the ^{55}Fe source stock solution ($t_{1/2}$ = 986 days, PerkinElmer Inc., USA, 1.7 MBq in 0.01 mL in 1 M HCl) to prepare tracer solutions at the required Fe concentrations. The pH of the C-S-H suspensions varied in accordance with the equilibrium conditions determined by the solid compositions (Ca/Si ratio of C-S-H phases) or by adjustment to higher pH with 1.0 M NaOH. The pH of the TiO_2 suspensions was adjusted with NaOH. For the kinetic experiments, the samples were equilibrated on the end-over-end shaker and regularly sampled up to 12 and 120 days in the case of TiO_2 and C-S-H suspensions, respectively.

Sorption isotherms were determined at three pH values for C-S-H 0.8 and C-S-H 1.5. In these experiments increasing volumes of $FeCl_3$ solutions (0.09 M, 0.02 M, and 0.008 M) labelled with ^{55}Fe (concentration active Fe/ inactive Fe = 3.5×10^{-7}) were added to the suspensions and shaken end-over-end for 40 days. The total initial Fe concentration used in isotherm experiments ranged from 4.3×10^{-3} M to 3.9×10^{-6} M. After equilibration, an aliquot of each suspension was withdrawn and diluted with HCl 0.01 M (HCl 0.1 M in case of the suspensions with pH > 13) in order to dissolve the solid phase. The remaining suspension was subjected to centrifugation (1h, 95,000 g) and the supernatant solution was sampled in triplicates and used for radio assay. ^{55}Fe activities in the acidified suspensions and the supernatant solutions were determined along with standards and blanks by liquid scintillation counting (LSC) using a Perkin Elmer Tri-Carb A2750 liquid scintillation analyser with energy windows set between 2-10 keV. Samples for LSC were prepared by mixing 5 mL aliquots of the acidified suspensions or the supernatant solutions with 15 mL scintillator (Ultima Gold XR, Packard Bioscience, USA). The solid contents (C-S-H, TiO_2) were too low to cause any significant quenching effects by remaining solid particles. Standards and blanks had the same solution compositions as the samples.

The speciation and solution as well as the solubility of $Fe(OH)_3$ and $Al(OH)_3$ were calculated using the Gibbs Energy Minimization (GEM) Selektor code (Kulik et al., 2013) along with the PSI thermodynamic database (Hummel et al., 2002; Thoenen et al., 2014) for Fe- and Al-hydroxides.

2.3 *^{29}Si NMR*

C-S-H samples with a Ca/Si ratio = 0.8 and 1.5 and loaded with 1000 ppm and 5000 ppm Fe were studied by ^{29}Si NMR. In addition, the corresponding Fe-free C-S-H were analysed as reference. The single-pulse ^{29}Si NMR spectra were acquired at 79.4 MHz on a Bruker Avance-II 400 spectrometer (9.4 T) using a 4 mm Bruker CP/MAS probe, PSZ (partially sintered zirconia) rotors and spinning speeds of ν_R = 4.0 kHz or 10.0 kHz. The experiments employed a (π/4) excitation pulse (τ_p = 1.75 µs for $\gamma B_1/2\pi \approx 70$ kHz) and a relaxation delay of 30 s. The saturation-recovery and spin-counting ^{29}Si NMR experiments were performed at 59.5 MHz on a Varian INOVA-300 spectrometer, employing a homebuilt CP/MAS probe for 7 mm o.d. PSZ rotors and a spinning frequency of ν_R = 7.0 kHz. The saturation-recovery

experiments used 12 saturation pulses (π/2, $\gamma B_1/2\pi \approx 40$ kHz) separated by 1.0 ms delays, prior to the recovery delay. The ^{29}Si chemical shifts are referenced to neat tetramethylsilane (TMS) using a sample of β-Ca_2SiO_4 (δ = -71.33 ppm) as a secondary reference.

2.4 Synchrotron-based investigations

2.4.1 Sample preparation

Fe K-edge XAS measurements were performed on Fe-doped C-S-H phases, CaO, SiO_2 and TiO_2. The C-S-H phases were synthesised according to the procedure described above. CaO, SiO_2, and TiO_2 were prepared with the same solid to liquid ratio used in the experiments (5 g/L for CaO and SiO_2, 0.2 g/L for TiO_2). CaO and SiO_2 chemicals were those used for the preparation of C-S-H phases. The pH of the suspensions was adjusted to 12.5 with 0.03 M NaOH. Appropriate volumes of $FeCl_3$ solutions (5×10^{-3} M) were added to the suspensions in order to achieve the target Fe loadings (typically > 500 ppm). The Fe-containing suspensions were equilibrated end-over-end up to 60 days. After equilibration, suspensions were centrifuged (1h, 95,000 g). The supernatant solutions were sampled for ICP-OES measurements, and the wet pastes were placed into Plexiglas sample holders and sealed with Kapton tape. All samples were sealed in ICP-OES vials, which contained a wetted water absorbent at the bottom, and stored inside a glove box with N_2 atmosphere to avoid drying-out and carbonation.

2.4.2 Data collection and fitting

XAS measurements were conducted at the Samba beamline (Soleil, Saint Aubin, France) and at the Dutch-Belgian beamline (Dubble - European Synchrotron Radiation Facility (ESRF), Grenoble, France). Both beamlines are equipped with a Si (111) crystal monochromator. The monochromator angle was calibrated by assigning the energy of 7112 eV to the first inflection point of the Fe K-edge spectrum of an iron foil. The measurements were performed at room temperature in transmission mode in case of the references using ionization chambers and in fluorescence mode in case of the Fe-loaded paste samples using the high-quality detectors available at the beamlines (Samba: Canberra 35-elements

monolithic planar Ge pixel array detector; Dubble: 9-elements monolithic detector). For each sample, several spectra were recorded, deglitched if necessary, and merged.

EXAFS (extended X-ray absorption fine structure) data reduction was performed by using the ATHENA software package (Ravel and Newville, 2005). Upon background subtraction the energy was converted to photoelectron wave vector units ($Å^{-1}$) by assigning the ionization energy of Fe K-edge (E_0 = 7112 eV) to the first inflection point of the absorption edge. Radial structure functions (RSFs) were obtained by Fourier transforming the k^3-weighted $\chi(k)$ spectra between 2.0 and 10.0 $Å^{-1}$ using a Kaiser-Bessel window function with a smoothing parameter of 4. Multi-shell fits were performed in the real space across the first three shells (ΔR = 1 to 5 $Å^{-1}$) to determine the structural parameters of the absorber atom (coordination number (N), bond length (R), Debye-Waller (σ^2) factor). Note that the fitting space for the references was reduced to 4 A^{-1}. Theoretical scattering paths were calculated using FEFF 8.2 (Ankudinov et al., 1998; Rehr et al., 1991) and structures of different minerals (described below) as model. The goodness of the fit was evaluated on the basis of the residual factor (R-factor). The amplitude reduction factor (S_0^2) was fixed to 0.83 as previously reported by Wang et al. (2016).

3 Results and discussion

The XRD and TGA patterns revealed that the main component of the synthesised C-S-H samples is a tobermorite-like material. The basal spacings of the C-S-H phases C-S-H 0.8 and C-S-H 1.5 were determined to be ~13.5 Å and ~11.0 Å, respectively. As expected, the interlayer decreases with increasing Ca/Si ratio because of the higher amount of Ca atoms in the interlayer and thus closer silica chains attracted by the positive charge of Ca (Geng et al., 2017; Lothenbach and Nonat, 2015; Renaudin et al., 2009).

3.1 Sorption experiments

The uptake of ^{55}Fe onto C-S-H phases and TiO_2 can be expressed in terms of a K_d value (distribution coefficient), which is commonly used to quantify the partitioning of a radiotracer between solid and liquid phase in case of linear sorption. The K_d value is defined as follows:

$$K_d = \frac{C_{s,eq}}{C_{l,eq}} = \frac{(C_0 - C_{l,eq})}{C_{l,eq}} \times \frac{V}{M} \qquad (m^3\ kg^{-1}) \qquad (1)$$

where $C_{s,eq}$ is the equilibrium Fe concentration traced via ^{55}Fe activity sorbed on C-S-H phases [mol kg^{-1}], $C_{l,eq}$ is the equilibrium concentration in solution [mol·m^{-3}]. The difference between the initial ^{55}Fe activity in suspension (C_0) and the activity determined in the supernatant ($C_{l,eq}$) corresponds to sorbed ^{55}Fe. M is the dry weight of the C-S-H phase [kg], and V is the volume of solution [m^3]. Note again that the dry weight corresponds to the sum of CaO and SiO_2 masses used to synthesise a C-S-H phase with the target Ca/Si ratio, meaning that water is disregarded in the mass calculations (Tits et al., 2006b). Isotherm data are presented as the quantities of Fe sorbed per kg solid (dry weight of C-S-H) versus the Fe equilibrium concentration. In addition, the Fe/Si mol ratios of the C-S-H phases are shown along the second y-axis.

The sorption studies were carried out at high ^{55}Fe activities (count rate of initial ^{55}Fe-containing suspension > 5 × 10^5 cpm/mL) in order to be able to quantify the K_d value on the basis of statistically significant count rates (Tits et al., 2002). The initial ^{55}Fe activity of the suspension (C_0) was determined from an aliquot withdrawn from the suspension prior to phase separation by centrifugation while the activity in solution ($C_{l,eq}$) was determined from an aliquot of the supernatant solution after phase separation. It was observed that the way the tubes were handled after centrifugation had an effect on the count rate and further on the scatter of the data. For example, small amounts of nanoparticles released from the solid to the supernatant solution after phase separation resulted in enhanced count rates of the supernatant solution and consequently lower sorption values leading to large experimental uncertainty on the sorption values (estimated ± 30%). Sorption of the ^{55}Fe tracer on the walls of the polyallomer centrifuge tubes was checked by mass balance calculations and found to be negligible at the given solid-liquid ratio of the C-S-H samples.

3.1.1 Fe sorption on TiO_2

Titanium dioxide (TiO_2) is known to have a low solubility and recrystallization rate and further to be chemically stable in alkaline conditions (Schmidt and Vogelsberger, 2009). Radionuclide incorporation into the chemical structure of this mineral is very unlikely, and

294 therefore TiO_2 is well suited to study radionuclide surface complexation behaviour in
295 alkaline conditions (Comarmond et al., 2011; Tits et al., 2014).

296 Kinetic experiments with ^{55}Fe on TiO_2 were carried out in NaOH solution (pH = 12.5)
297 at a total Fe concentration of 10^{-8} M, which is below the solubility limit with respect to
298 microcrystalline $Fe(OH)_3$(mc) under these conditions. The results showed that the chemical
299 equilibrium was reached within 3 days (see Fig. S1 in Supplementary Information (SI)). The
300 K_d value was estimated to be 32 m^3/kg from these kinetic studies.

301 The isotherm measurements showed that Fe sorption onto the TiO_2 surface is linear
302 at low Fe concentrations while Fe(III)-hydroxide precipitation occurred at higher
303 concentrations (Fig. 1a). The K_d value in the linear range of the sorption isotherm was
304 estimated to be 68 m^3/kg, which is consistent with the K_d value determined from the kinetic
305 experiments within the experimental uncertainty. Above an aqueous Fe concentration of 10^{-7}
306 M (dashed vertical line in Fig. 1a), precipitation of $Fe(OH)_3$(mc) occurred which is in line
307 with thermodynamic calculations showing that the solubility limit of amorphous Fe-
308 hydroxide is about three orders of magnitude higher than that of microcrystalline Fe-
309 hydroxide (Table 1).

310 **Table 1** Solubility limits for amorphous and microcrystalline $Fe(OH)_3$. Thermodynamic data
311 were taken from Thoenen et al. (2014).

	Solubility limit (mol/L)	
pH	*amorphous*	*microcrystalline*
11.5	1×10^{-5}	1×10^{-8}
12.5	1×10^{-4}	1×10^{-7}
13.0	3×10^{-3}	3×10^{-6}
13.5	1×10^{-3}	1×10^{-6}

312

313 $Fe(OH)_4^-$ is the main species in solution under the highly alkaline conditions of C-S-H
314 systems and its fraction increases with pH (Fig. S2 in SI). Fe uptake by TiO_2 was observed to
315 decrease with increasing pH (Fig. 1b). The effect of Fe hydrolysis on sorption was modelled
316 in terms of a sorption reduction factor (F_{red}) (solid line in Fig. 1b). The latter factor accounts
317 for the partitioning of Fe between solid and liquid phase which is pH dependent due to the
318 formation of $Fe(OH)_4^-$. The pH dependent reduction of the K_d value was calculated from
319 Eq.(2):

$$F_{red} = \frac{K_d^0}{K_d} = 1 + \left(\frac{{}^{*}K_2'}{[H^+]}\right), \quad (2)$$

where K_2' corresponds to the stepwise stability constant of the following reaction at a given ionic strength (Table 2):

$$Fe(OH)_3\ (aq) + H_2O = Fe(OH)_4^- + H^+$$

Table 2: Stepwise stability constants for the Fe(III)-hydroxyl species used in the model at I = 0. $Log^*K_4^0 = log^*\beta_4^0 - log^*\beta_3^0$. Thermodynamic data were taken from Thoenen et al. (2014). Notation was chosen according to the sequence of hydrolysis reactions.

Species	$Log^*\beta_n^0$	$Log^*K_4^0$
$Fe(OH)_3$	-12.56	
$Fe(OH)_4^-$	-21.60	-9.04

The good agreement between modelled and experimental data implies that the decrease in the K_d value results from increasing $Fe(OH)_4^-$ concentrations in solution (Fig. 1b). Thus, for surface complexation as dominant mechanisms, we may anticipate that Fe uptake decreases with increasing pH in the typical range of cement systems 10.5 < pH < 13.5.

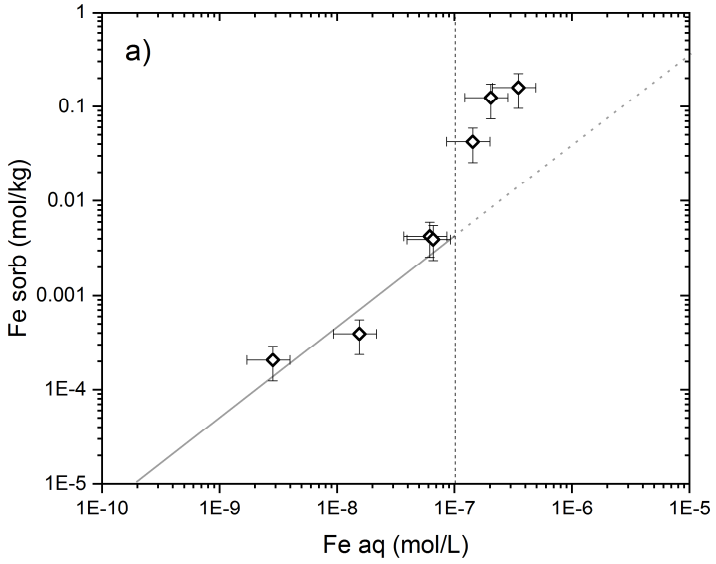

334

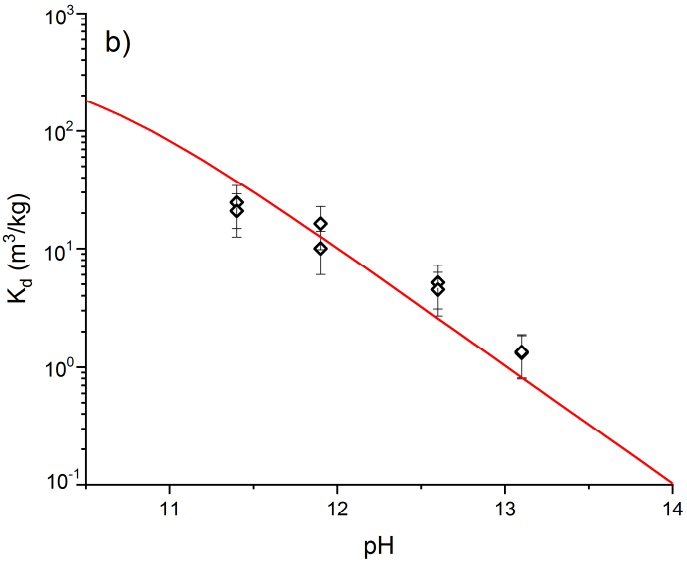

335

336 **Figure 1:** a) Sorption isotherm of Fe on TiO_2 (pH 12.5); the dotted vertical line indicates the
337 stability field of $Fe(OH)_3$(mc), b) pH dependence of Fe sorption on TiO_2.The solid line was
338 modelled by considering the sorption reduction factor defined in Eq. (2). The total Fe
339 concentration in the samples amounts to 10^{-8}M.

340 *3.1.2 Fe sorption on C-S-H*

341 The Ca/Si ratio of C-S-H phases in cement pastes typically ranges between 0.8 and
342 1.6 (Deschner et al., 2012; Taylor et al., 2010). Low Ca/Si ratios are observed in cement
343 pastes if Si-rich supplementary material is added to the initial cement mixture (Lothenbach

et al., 2011). Sorption experiments were performed with C-S-H phases that cover the typical range of Ca/Si ratios, i.e. Ca/Si ratios = 0.8, 1.2 and 1.5. The kinetic experiments showed that the chemical equilibrium of Fe uptake is attained within 30 days (Fig. S1 in SI). The mean K_d value was estimated by averaging all K_d values determined in the kinetic experiments after attaining equilibrium conditions and from the isotherm measurements (Table 3 and Table S1 in SI). Note that the uncertainty on the data was large due to the large scatter in the experimental data. The K_d values (expressed in terms of m^3/kg) of all C-S-H phases were similar within the uncertainty range. They were normalized to surface area (expressed in terms of L/m^2) in order to account for different specific surface areas of the C-S-H phases. Sunda et al. (2015) observed that the surface area of C-S-H phases decreased with increasing Ca/Si ratio. In this study we used an upper estimate for the surface area of C-S-H 1.5 which was based on experiments at Ca/Si = 1.4. (Suda et al., 2015). The surface-normalized mean K_d value seems to increase with increasing Ca/Si ratio of the C-S-H phases but the trend is statistically not significant. The K_d values of the C-S-H phases, however, are significantly higher than TiO_2 indicating that Fe uptake by C-S-H phases is stronger than by TiO_2 and that other mechanisms in addition to surface complexation may be important.

Table 3: K_d values experimentally determined and normalized with respect to the surface area.

	Surface area (m^2/g)	**K_d (m^3/kg)** *experimental*	**K_d (L/m^2)** *normalized*
C-S-H 0.8	333[a]	710 ± 148	2.1 ± 0.5
C-S-H 1.2	214[a]	698 ± 175	3.3 ± 0.8
C-S-H 1.5	193[a*]	679 ± 151	3.5 ± 0.8
TiO_2	56[b]	50 ± 18	0.9 ± 0.3

a) Suda et al, 2011; * value for C-S-H phase with Ca/Si ratio = 1.4
b) Schmidt and Vogelsberg, 2009; Comarmond et al., 2011

Sorption isotherms were determined for the C-S-H phases with Ca/Si ratios = 0.8 and 1.5. The Fe sorption behaviour was linear over the entire aqueous Fe concentration range for both C-S-H phases (slope = 1) (Fig. 2). In contrast to sorption onto TiO_2, Fe uptake by C-S-H phases linearly increased over the entire investigated Fe concentration range, implying

that formation of the solubility-limiting phase microcrystalline $Fe(OH)_3$ was not observed. Precipitation of amorphous $Fe(OH)_3$(am) presumably occurred at higher Fe concentrations in the system with C-S-H 0.8 as the data at higher Fe loadings slightly deviate from the linear trend of the sorption isotherms (Fig. 2).

The results showed that neither the C-S-H composition nor the pH have any notable effect on Fe sorption. The sorption data for C-S-H 0.8 and 1.5 coincide within the experimental uncertainty (Fig. 2). Note that a significant pH effect has been anticipated on the basis of the pH dependence of Fe uptake by TiO_2 (Fig. 2 solid line) and because a strong decrease of uptake was observed with increasing pH in the case of Al(III) (Barzgar et al., 2019). For Al(III), also an increase of uptake at higher Ca/Si was observed experimentally (L'Hôpital et al., 2016), which was related to an ordering effect of Ca on Al binding in the interlayer (Barzgar et al., 2019). For Fe in C-S-H phases, however, the effect of pH is negligibly small or even absent suggesting that in addition to surface complexation, other Fe uptake mechanisms may be important. The different effect of pH and Ca on Al(III) and Fe(III) uptake indicates that Fe has a different binding mechanism in C-S-H than Al(III) because Al(III) in tetrahedral coordination replaces Si(IV) at the bridging position of the dreierketten silica chains. The extent of Fe uptake, however, seems not to depend strongly on the Ca/Si ratio and accordingly the C-S-H structure.

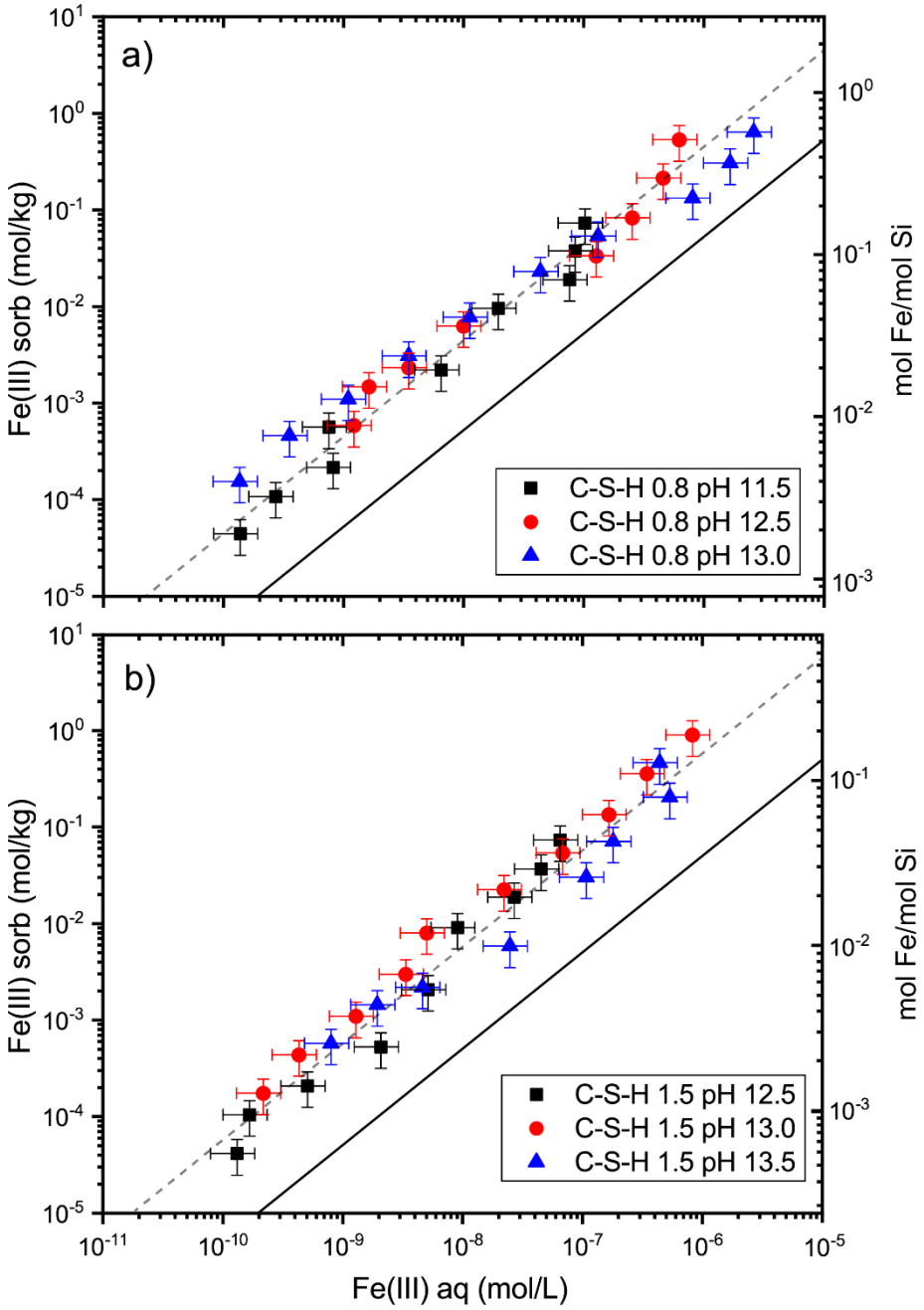

387

388 **Figure 2:** Sorption isotherms of Fe on C-S-H 0.8 (a), and C-S-H 1.5 (b). The experimental data
389 showed a linear sorption (slope = 1 of the dashed lines). The x-axis are the same for figure a)
390 and b). The left vertical axis indicates the sorbed Fe concentration, while the molar ratio of
391 Fe sorbed to Si of C-S-H is shown along the right vertical axis. Calculated solubility limits for
392 Fe-hydroxide are summarised in Table 1. The solid lines show the hypothetical positions of
393 the sorption isotherm at pH 13 (C-S-H 0.8) and 13.5 (C-S-H 1.5) under the assumption that
394 the presence of $Fe(OH)_4^-$ (Eq.(2)) leads to the same sorption reduction as observed on TiO_2.

395

3.2 ^{29}Si NMR

Iron-loaded (0, 1000 and 5000 ppm) C-S-H 0.8 and C-S-H 1.5 (Fig. S3 in SI) were equilibrated for 30 days. The ^{29}Si MAS NMR spectrum of the Fe-free C-S-H 0.8 sample (Fig. 3) allowed identification of resonances from the Q^1 , Q^2_b, and Q^2_p tetrahedral SiO_4 sites of the C-S-H structure at -79.4, -83.6 and -85.3 ppm, respectively, where the Q^2_b resonance is seen as a shoulder to the Q^2_p peak. Q^2_p and Q^2_b identifies silica in the pairing and bridging positions of the dreierketten structure, while Q^1 sites are dimers and end-of chain silica sites. The Q^2_b resonance was not resolved in the corresponding spectrum of the C-S-H 1.5 sample, which was dominated by the Q^1 and Q^2_p resonances at -79.1 ppm and -84.6 ppm, respectively. A determination of the relative peak intensities from simulations of the spectra allowed calculation of the average mean chain lengths (MCL) of silicate tetrahedra, giving the values MCL = 17.9 for C-S-H 0.8 and MCL = 2.6 for C-S-H 1.5, which are typical values for C-S-H samples with low and high Ca/Si ratios (Richardson, 2014).

The resolution of the centerband resonances in the -75 to -87 ppm region was rather similar for the samples with and without Fe. The main difference is a small increase in linewidth for the Q^1 resonance of the C-S-H 1.5 samples on going from Fe-free conditions, FWHM = 2.1 ppm, to the samples with 1000 ppm Fe (FWHM = 2.6 ppm) and 5000 ppm (FWHM = 2.8 ppm). However, a similar effect was not observed for the C-S-H 0.8 sample, where the Q^2_p peak exhibits a linewidth of ~2.4 ppm for all samples. The most clear reflection in the ^{29}Si NMR spectra of Fe in the samples (Fig. 3) is the increasing intensities of the spinning sidebands, observed at approx. 16, -32, -130, and -180 ppm, the effect being most pronounced for Ca/Si = 1.5 with increasing Fe content. Following an earlier ^{29}Si NMR study of Fe in anhydrous Portland cements (Poulsen et al., 2009), these spinning sidebands are associated with the dipolar coupling between the magnetic moments of the unpaired electrons from Fe and the nuclear spin of ^{29}Si. This interaction is inversely proportional to the cube of the distance between the unpaired electron and the ^{29}Si nucleus ($1/(r_{e-^{29}Si})^3$). Thus, the Fe ions are in a closer vicinity to Si sites in the high Ca/Si sample as compared to low Ca/Si.

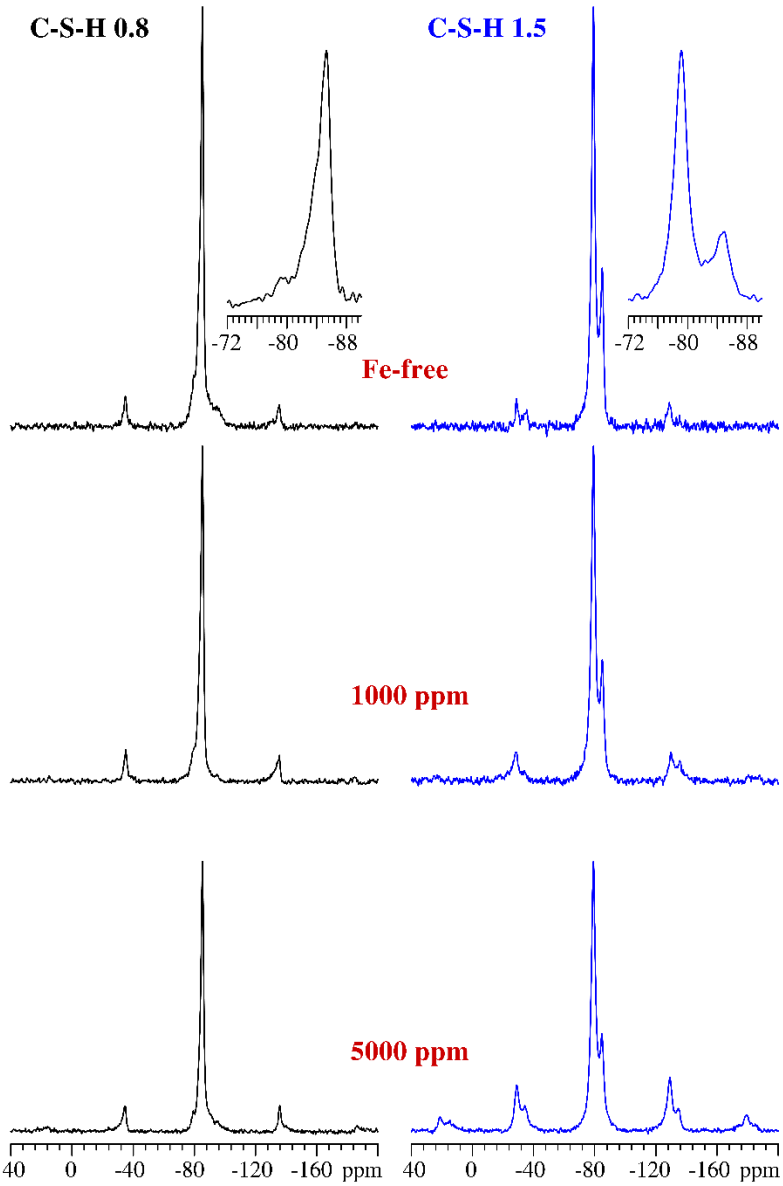

Figure 3: ^{29}Si MAS NMR spectra of the C-S-H 0.8 (black) and C-S-H 1.5 (blue) samples that are, from top to bottom, Fe-free and loaded with 1000 and 5000 ppm Fe. The spectra employ a spinning speed of 4.0 kHz except for insets of the Fe-free samples, which correspond to a spinning speed of 10.0 kHz, where all intensity is gathered in the shown centerbands from approx. -75 to -87 ppm.

The magnetic moment of the electron spin was approx. 3300 times larger than the nuclear ^{29}Si spin moment. Therefore, the coupling between these spins also provides a very efficient dipolar relaxation mechanism for the ^{29}Si magnetization, proportional to $1/(r_{e-^{29}Si})^6$. For Fe in the nearest environment to ^{29}Si, this may result in decay of the free

induction decay (FID) within a few tens of microseconds and thereby partly during the dead-time between the radio-frequency (rf) pulse and the acquisition of the FID in single-pulse NMR experiments. A measure for the signal reduction, caused by efficient relaxation by the unpaired electrons of Fe(III), can be obtained by 'spin-counting' single-pulse ^{29}Si NMR experiments, where the signal intensity is compared (for weighed samples) in fully- relaxed ^{29}Si NMR spectra. Using this approach, and the spectra of the Fe-free C-S-H samples as intensity reference (I_0), results in the reduction in signal intensities (I) listed as normalized intensities in Table 4. These I/I_0 values are very similar for the Q^2 sites of C-S-H 0.8 and the Q^1 sites of C-S-H 1.5, *i.e.*, roughly 95% and 90% at Fe contents of 1000 and 5000 ppm, respectively. However, at significantly stronger effect is seen for the Q^2 sites of C-S-H 1.5, indicating that the Fe ions are closer to these sites in the C-S-H 1.5 structure as compared to the Q^1 sites.

Table 4: ^{29}Si spin-lattice relaxation times (T_1 and T_1') from saturation-recovery NMR experiments and normalized intensities (I/I_0) from spin-counting NMR for the C-S-H 0.8 and C-S-H 1.5 samples with different levels of Fe.*

Ca/Si	Fe(III) (ppm)	Si site	T_1 (s)	T_1' $(s^{1/})^2$	I/I_0 (%)
0.8	0	Q^2	94 ± 4	-	100
	1000	Q^2	-	3.7 ± 0.4	95.3
	5000	Q^2	-	5.5 ± 0.6	89.1
1.5	0	Q^1	67 ± 4	-	100
		Q^2	77 ± 5	-	100
	1000	Q^1	-	0.234 ± 0.013	94.3
		Q^2	-	0.160 ± 0.008	82.6
	5000	Q^1	-	0.060 ± 0.003	91.6
		Q^2	-	0.036 ± 0.003	68.7

* The ^{29}Si NMR experiments were performed at 7.05 T. The spin-lattice relaxation times was determined from single-exponential fits for the Fe-free samples and from a stretched exponential relationship for the Fe(III) containing samples, providing the relaxation times, T_1 and T_1', in s and $s^{1/2}$, respectively (see section 3.2).

Further evidence for these trends was obtained by a determination of the ^{29}Si spin-lattice relaxation times (T_1) for the Q^1 , Q^2 sites in the individual C-S-H samples, employing the saturation-recovery pulse sequence (Markley et al., 1971). The latter parameter is

conveniently used for samples exhibiting very long relaxation times. In the absence of paramagnetic ions, the evolution of the ^{29}Si magnetization, as a function of the recovery time (τ), follows a single-exponential relationship, $M_z(\tau) = M_0[1 - \exp(-\tau/T_1)]$, allowing the determination of the conventional spin-lattice relaxation time, T_1. However, this relationship does not hold in presence of paramagnetic ions, as a result of the strong unpaired electron – nuclear spin dipolar couplings, where a 'stretched exponential' relationship may alternatively be used, $M_z(\tau) = M_0[1 - \exp(-(\tau/T_1')^{1/2})]$ (Tse and Hartmann, 1968). This stretched exponential relation has been successfully used in ^{29}Si NMR studies of silicate minerals containing small amounts of paramagnetic ions (e.g., Fe^{3+}, Co^{2+}, Ni^{2+}, Co^{2+},) (Hartman and Sherriff, 1991; Hartman et al., 2007) and of the alite and belite phases in Portland cements (Poulsen et al., 2009; Skibsted et al., 1995). As an example, Figure 4 illustrates the ^{29}Si magnetization as a function of the recovery time for Fe-free C-S-H 1.5 and the sample including 1000 ppm Fe along with the optimized fits using the single-exponential and stretched exponential relationships, respectively. The resulting spin-lattice relaxation times, T_1 (s) and T_1' ($s^{1/2}$), are summarized in Table 4. Rather long T_1 values were observed for both Fe-free samples, as generally found for silicate minerals in the absence of paramagnetic ions. For the Fe containing samples, the T_1' values were markedly longer for C-S-H 0.8 as compared to C-S-H 1.5 at both Fe concentrations. Furthermore, the T_1' values were shorter for the Q^2 site as compared to the Q^1 environments in C-S-H 1.5, supporting the result from the spin-counting ^{29}Si NMR experiments. This indicates that Fe ions are in a nearer environment to the Q^2 sites as compared to the dimers and end-group Q^1 sites.

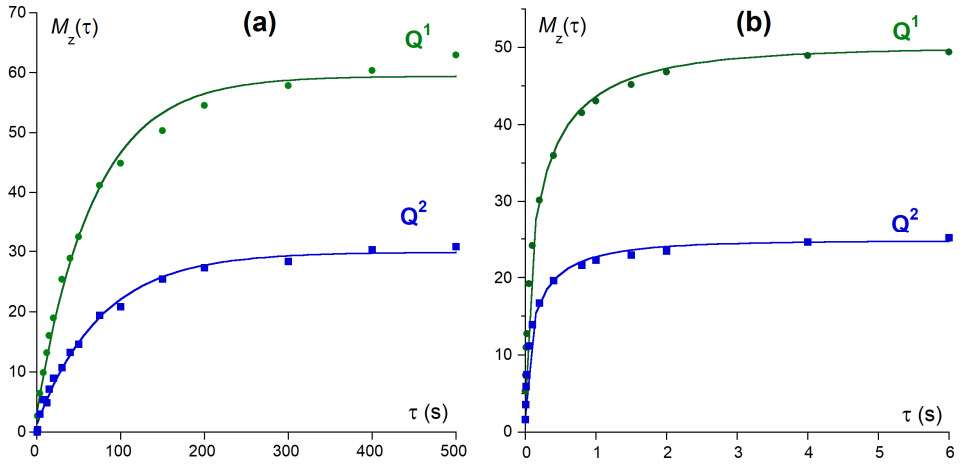

Figure 4: The observed magnetization, $M_z(\tau)$, as a function of the recovery time (τ) in saturation-recovery ^{29}Si NMR experiments for C-S-H 1.5 including (a) no Fe, and (b) 1000 ppm Fe. The curves correspond to (a) single-exponential and (b) stretched-exponential fits to the data, resulting in the T_1 and T_1' relaxation times, respectively, listed in Table 4. The $M_z(\tau)$ values are shown on arbitrary intensity scales. Note the different τ-axes in (a) and (b).

3.3 XAS spectroscopy

Iron-loaded C-S-H samples were equilibrated up to 60 days and analysed by Fe K-edge absorption spectroscopy. Three different Fe loadings were applied to the C-S-H phases with Ca/Si ratios = 0.8 and 1.5 (600 ppm, 12,000 ppm, and 50,000 ppm) and the C-S-H phase with Ca/Si ratio = 1.2 (900 ppm, 15,000 ppm, and 60,000 ppm) (Fig. S3 in SI). In addition, CaO, SiO_2, and TiO_2 were loaded with 600 ppm Fe and analysed.

3.3.1 Comparison of coordination environments of Fe in C-S-H and references

Normalized XANES spectra are displayed in Figure 5a. All spectra showed pre-edge features at 7114.5 eV, which are caused by electronic transition from the 1s to 3d states in the iron atom (Wilke et al., 2001). The intensity and shape of the pre-edge reflect the coordination environment of Fe, i.e. low intensity for octahedral and strong intensity for tetrahedral sites (Wilke et al., 2001). The strongest pre-edge was observed in the SiO_2 spectra, while for the other samples the intensity of the pre-edge was similar although significantly weaker as compared to SiO_2. Thus, the pre-edge features suggest that Fe bound to SiO_2 is located in a tetrahedral coordination environment, whereas an octahedral

coordination environment is expected for all the other samples (the spectrum of TiO_2 is reported in Fig. S4). This observation is in line with the results reported by Pokrovski et al. (2003) who investigated the influences of aqueous silica on the hydrolyses of Fe. These authors showed that the intensity of the pre-edge increases with increasing silica concentration, indicating a higher presence of tetrahedral Fe in the solution.

The effect of time on Fe uptake was investigated for C-S-H 0.8 and 1.5 with low Fe loadings (600 ppm). Figure 5b shows the radial structure function (RSF) of the samples equilibrated for 1 and 30 days. The C-S-H 1.5 sample revealed a strong peak at R+ΔR ~ 2.95 Å after one day of equilibration. This backscattering contribution was not observed at the given position after 30 days (long dashed line in Fig. 5b) while a strong backscattering contribution appeared at R+ΔR ~ 3.12 Å. In C-S-H 0.8, the sample equilibrated for one day showed a peak at R+ΔR ~ 3.05 Å, whose intensity was much less after 30 days. The differences in the intensities of the spectra in the samples after 1 and 30 days reaction reveal differences in the coordination environments as further discussed in section 3.3.2. The kinetic experiments showed that the equilibrium state of the uptake process is reached within 30 days (in agreement with wet chemistry experiments), suggesting that the coordination environments determined after 30 days are representative of the thermodynamically stable Fe speciation in the C-S-H systems.

The backscattering contribution observed at R+ΔR ~ 2.95 Å in the C-S-H 1.5 spectrum after one day was also visible in the CaO spectrum. This finding suggests that Fe coordination to Ca atoms occurred initially on the C-S-H surface. Nevertheless, the coordination number and distance of the neighboring Ca atoms was different after 30 days as indicated by the peak shift. This finding shows that, in the long term, a mechanism different from coordination to Ca atoms on the C-S-H surface accounts for Fe uptake. The Fourier transformed (FT) spectrum of Fe-loaded SiO_2 showed much weaker backscattering contributions as compared to those of the Fe-loaded CaO and C-S-H phases. It should be noted that the FT of the Fe-loaded SiO_2 sample revealed spectral features that were similar to those of C-S-H 0.8 after 30 days. The FT showed two small peaks at 2.30 Å and 2.70 Å and a peak at 3.20 Å with a slightly higher intensity (short dashed line in Fig. 5b). The backscattering contribution at the two shorter distances are clearly visible in the C-S-H 0.8 sample after 30 days while the peak at the longest distance could be present both in the FT

of the C-S-H 0.8 and C-S-H 1.5 samples after 30 days. This finding suggests Fe coordination to neighboring Si atoms in both C-S-H 0.8 and 1.5 samples.

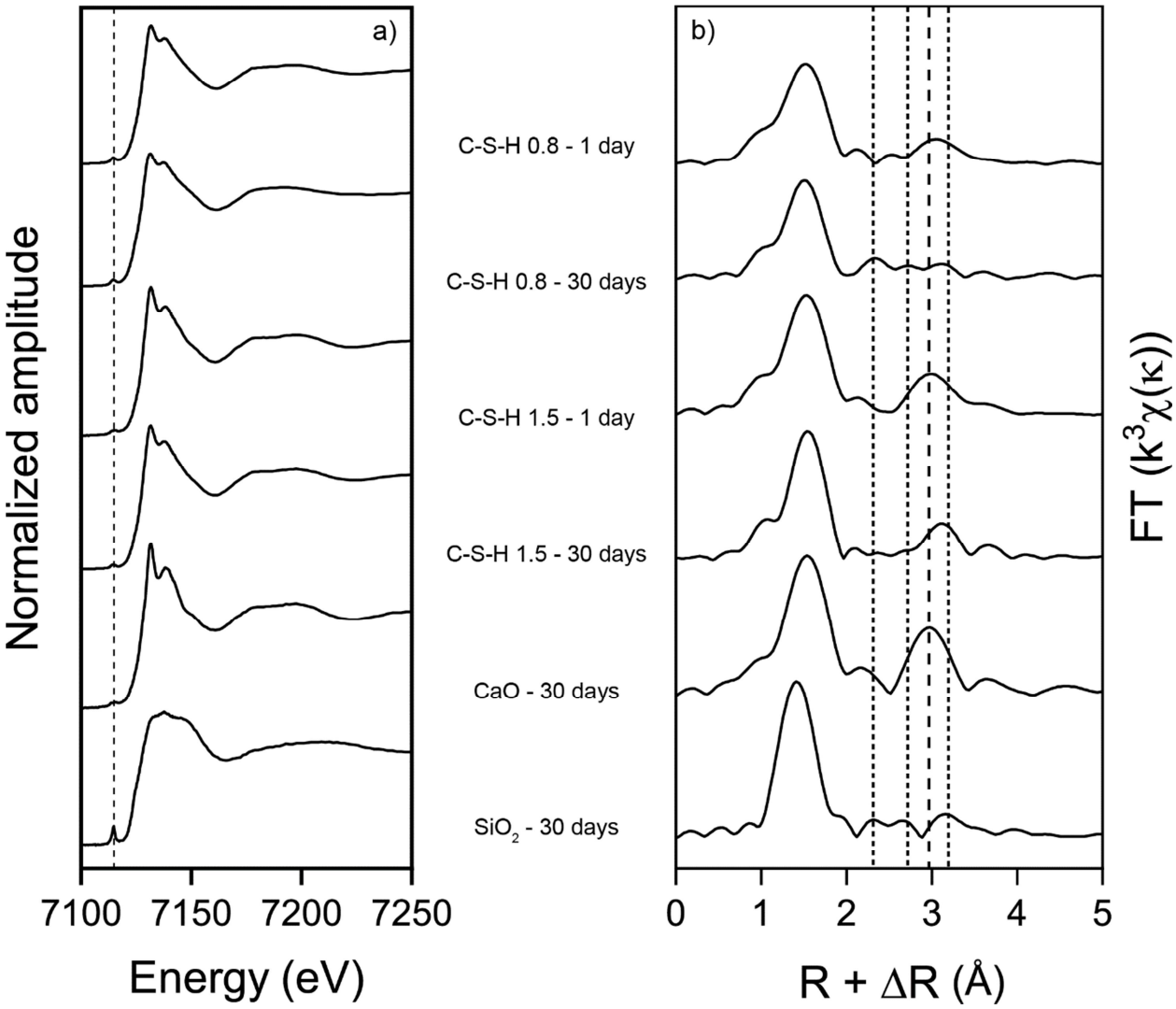

Figure 5: a) Fe-K edge spectra and b) Fourier transforms of Fe sorbed on C-S-H 0.8 and 1.5, CaO, and on SiO_2 at different equilibration times (Fe loadings = 600 ppm). The dotted line in panel a) highlights the pre-edge feature at 7114.5 eV. In panel b) the dotted lines indicate 2.30 Å, 2.70 Å, and 3.20 Å and the dashed line refers to 2.95 Å.

A multi shell fitting approach was applied to determine the structural parameters for Fe bound to CaO, SiO_2 and TiO_2 (Fig. 6 and Table 6). The SiO_2 spectra was fitted by replacing an Al by a Fe atoms in a zeolite structure (Gualtieri and Passaglia, 2006). The first backscattering peak corresponds to the nearest O shell. Fe was found to be surrounded by

four O atoms reflecting a tetrahedral geometry, as already suggested by the strong pre-edge (Fig. 5a). The Fe-O distance was determined to be 1.85 ± 0.01 Å. The second and the third shells were fitted by considering Si and O backscattering contributions, respectively. The Debye-Waller factor for Si was fixed for the goodness of the fit. The best fit was achieved with two Si atoms at a distance of 3.20 ± 0.02 Å, and four O atoms at 3.61 ± 0.02 Å indicating surface complexation of Fe.

The CaO spectrum was fitted by considering 6 O atoms. This reflects an octahedral coordination environment, which is again in agreement with the pre-edge feature. Note that the Fe-O distance in octahedral coordination is longer than in tetrahedral coordination. A second backscattering contribution caused by the presence of 4 Ca atoms in the second shell (3.47 ± 0.02 Å) was observed. The fitting could not be improved by considering further contributions. The large number of neighboring Ca atoms suggest incorporation into a CaO structure rather than surface complexation.

Determination of the sorption isotherm on TiO_2 showed linear Fe sorption up to 300 ppm (0.005 mol/kg; Fig. 1a). It should be noted that the EXAFS sample prepared with a Fe loading of 600 ppm on TiO_2 was supersaturated with respect to microcrystalline $Fe(OH)_3$(mc). In fact, the spectrum showed features similar to that of $Fe(OH)_3$, for example the small peak at k ~ 7.5 $Å^{-1}$ and the backscattering contribution at ~ 2.7 Å. In addition, a multi-shells fit provided structural parameters that were similar for Fe bound to TiO_2 and $Fe(OH)_3$ within experimental errors (Table 5).

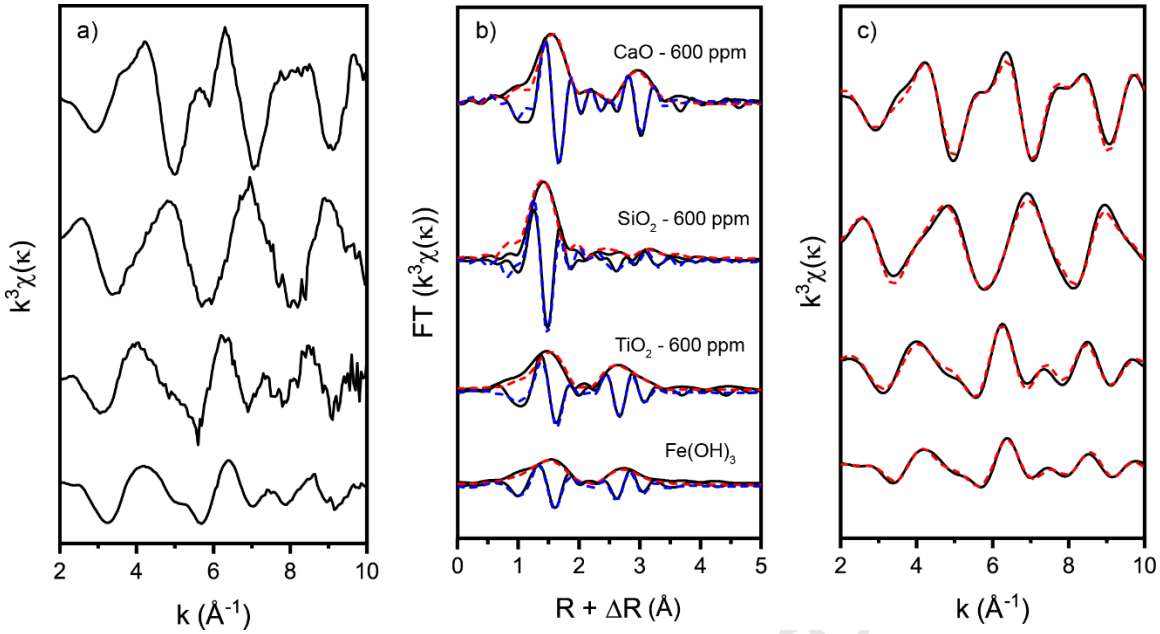

Figure 6: a) Fe K-edge spectra of CaO, SiO_2, and TiO_2 loaded with Fe and of $Fe(OH)_3$, b) corresponding Fourier transform of experimental (black solid line) and fitted spectra (colored dashed lines), c) k^3-weighted EXAFS function for the Fourier-backtransform spectra obtained from Fig. 6b.

Table 5: Structural parameters derived from EXAFS Fe K-edge data analysis of CaO, SiO_2, TiO_2, and $Fe(OH)_3$. Calculated uncertainties are given in parentheses. N = number of neighboring atoms, R = interatomic distance, σ^2 = Debye-Waller factor, ΔE = energy shift, R – factor = residual factor.

Sample	Fe(III) (ppm)	Shell	N	R (Å)	σ^2 ($Å^2$)	ΔE (eV)	R-factor
CaO	600	Fe-O	6*	2.02 (.02)	0.005 (.002)	-0.69 (1.5)	0.002
		Fe-Ca	3.9 (1.6)	3.47 (.02)	0.004 (.002)		
SiO_2	600	Fe-O	4.8 (.3)	1.85 (.01)	0.004 (.001)	8.51 (.9)	0.003
		Fe-Si	1.4 (.4)	3.20 (.02)	0.003*		
		Fe-O	3.7(1.2)	3.61(.02)	0.002 (.001)		
TiO_2	600	Fe-O	4.5 (1.1)	2.00 (.02)	0.008 (.004)	1.34(1.8)	0.004
		$Fe\text{-}Fe_1$	5.9 (1.0)	3.07 (.02)	0.013 (.006)		
		$Fe\text{-}Fe_2$	3.0*	3.46 (.08)	0.020 (.015)		
$Fe(OH)_3$	-	Fe-O	5.5 (.6)	1.96 (.03)	0.014 (.005)	-0.21 (1.3)	0.001
		$Fe\text{-}Fe_1$	4.0 (.8)	3.03 (.03)	0.015 (.002)		
		$Fe\text{-}Fe_2$	3.9 (.8)	3.42 (.03)	0.006*		
$Fe(OH)_3$ [a)]	-	$Fe\text{-}Fe_1$	4.5	3.01			
		$Fe\text{-}Fe_2$	3.9	3.43			

*) Fixed parameters

[a)] Manceau and Drits, 1993

3.3.2 Structural models for Fe uptake by C-S-H phases

The EXAFS spectra of the Fe-loaded C-S-H samples were significantly different in some key features. This prompted us to distinguish two types of coordination environments. The type 1 coordination environment was observed for C-S-H 1.2 and 1.5 samples at low Fe loadings, and at intermediate Fe loading in case of the C-S-H 1.5 sample. The main features of the corresponding spectra were the double peak at $k^3 \sim 3.8$ Å^{-1} and a small peak at $k^3 \sim 5.7$ Å^{-1} (Fig. 7) while the RSFs showed a peak at R+ΔR ~ 3.1 Å. The features were less pronounced for C-S-H 0.8 at low Fe loadings. In contrast, the type 2 coordination environment was observed for the samples with intermediate Fe loading on C-S-H 0.8 and 1.2 and at the highest Fe loadings for all C-S-H phases. These spectra showed features similar to those observed in the $Fe(OH)_3$ spectrum. These findings suggest that formation of $Fe(OH)_3$ dominated the structural arrangement of Fe in these samples.

Multi-shell fitting was performed by taking into account the type 1 and 2 classification. In case of the type 1 coordination environment, the 11 Å tobermorite structure was used to model the EXAFS spectra of the C-S-H 1.2 and 1.5 at low Fe loadings (Merlino et al., 1999). ^{29}Si NMR revealed that the position of Fe is likely close to the silica chain at high Ca/Si ratio, and therefore a structural model was developed which was based on the replacement of Ca by Fe in the interlayer (see section 3.3.2.1). Such a replacement is less likely for the C-S-H 0.8 sample according to the ^{29}Si NMR data and further, a different structural model was required to fit the EXAFS data of C-S-H 0.8 at low Fe loading (see section 3.3.2.2). Indeed, attempts made to fit the EXAFS data of Fe-loaded C-S-H 0.8 by considering Ca-Fe replacement in the tobermorite structure were not successful. The structural model to fit the type 2 coordination environment was based on the Fe-hydroxide structure (see section 3.3.2.3).

3.3.2.1 Type 1 coordination environment of C-S-H 1.2 and 1.5 at low Fe loading

All FTs showed a pronounced peak at R+ΔR ~ 1.7 Å, which corresponds to the backscattering contribution from the nearest oxygen shell (Fig. 7). The structural parameters were similar for this shell in all samples (Table 6). The number of neighboring oxygen atoms (N_O) was found to vary between 5.5 ± 0.6 and 6.7 ± 1.6, thus indicating octahedral

coordination. The Fe-O distance (R_{Fe-O}) was very close to 2.00 Å in all samples while the Debye Waller factor (σ^2) varied slightly between 0.004 ± 0.001 $Å^2$ and 0.006 ± 0.001 $Å^2$.

For the C-S-H phases with Ca/Si ratio 1.2 and 1.5, the presence of backscattering atoms at farther distances was indicated by the peaks at R+ΔR ~ 3.6 Å and ~ 4.3 Å, which could accurately be fitted by considering Fe-Si and Fe-Ca backscattering contributions. About four neighboring Si atoms were determined at R_{Fe-Si} 3.56 ± 0.03 Å (low Fe loading) and 3.62 ± 0.01 Å (intermediate Fe loading). Four neighboring Si were also found by Gaona et al. (2011) in case of Np(IV) uptake into C-S-H. The number of neighboring Ca atoms was determined to be 2.2 ± 0.5 in the C-S-H 1.5 sample with 600 ppm Fe loading. In order to reduce the residual, some parameters for Si and Ca were fixed in case of the C-S-H 1.2 sample with the 900 ppm as well as the C-S-H 1.5 sample with 12,000 ppm Fe loading, such as Debye-Waller factors and coordination numbers of Ca in C-S-H 1.5, and the coordination numbers of Si and Ca in C-S-H 1.2.The fixed parameters corresponds to those derived for the sample with 600 ppm Fe loading (Table 6). However, the fitting approach seems to be justified with a view to the resulting Fe-Ca and Fe-Si distances (e.g. for C-S-H 1.2 R_{Fe-Ca} = 3.56 ± 0.03 Å, R_{Fe-Ca} = 4.34 ± 0.03 Å; and for C-S-H 1.5 R_{Fe-Si} = 4.35± 0.04 Å), which are consistent with those of the C-S-H 1.5 sample with 600 ppm Fe loading (R_{Fe-Si} = 3.57 ± 0.01 Å and R_{Fe-Ca} = 4.36 ± 0.03 Å).

The fits could further be improved by considering a second oxygen shell. About 15 oxygen atoms were determined at R_{Fe-O2} between 4.43 ± 0.01 Å and 4.45 ± 0.03 Å. The number of second shell oxygen atoms is consistent for the three Fe-loaded C-S-H samples. The presence of water molecules in the interlayer of C-S-H phases accounts for the relatively large number of neighboring oxygen atoms at farther distance. The exact number of water molecules in the structure of C-S-H phases may depend on drying conditions (Allen et al., 2007; Bayliss, 1975; Brunauer, 1972; Gutteridge and Parrott, 1976; Roosz et al., 2017; Smith and Bayliss, 1972).

A structural model for Fe coordination in the interlayer of the C-S-H samples with Ca/Si = 1.2 and 1.5 can be proposed on the basis of the structural parameters deduced from EXAFS spectroscopy and supported by the ^{29}Si NMR data (Fig. 8) by considering the substitution of Ca by Fe in the interlayer of C-S-H phases. Atomic distances and numbers of neighboring atoms indicate that Fe is directly bonded to Si tetrahedra of the dreierketten silica chains adjacent to the interlayer space. The ^{26}Si NMR results showed that Fe in C-S-H phases with a

high Ca/Si ratio interacts more strongly with the Q^2 sites as compared to the Q^1 sites, thus indicating direct connection to the silica chain.

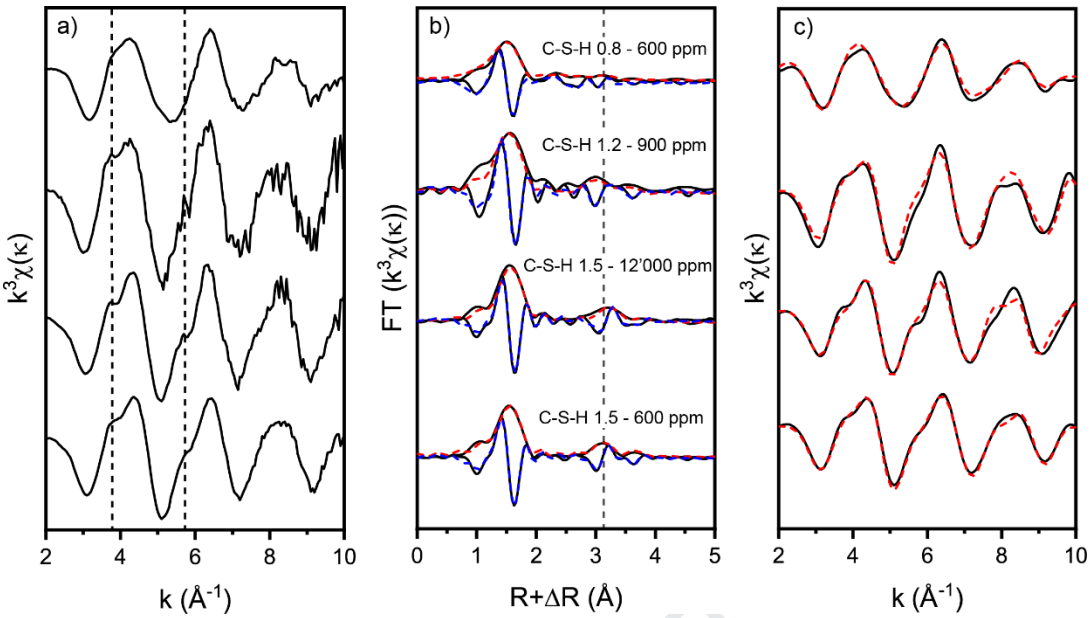

Figure 7: Experimental Fe K-edge spectra of Fe-doped C-S-H phases showing type 1 coordination environment (except for C-S-H 0.8). a) k^3-weighted spectra and b) the corresponding Fourier transform of experimental (black solid line) and fitted (colored dashed lines), and c) the k^3-weighted EXAFS function of the Fourier-backtransform spectra obtained from Fig. 7b. The coordination environment of Fe in the C-S-H phase with Ca/Si = 0.8 was fitted by considering a separate phase (see section 3.3.2.2).

Table 6: Structural parameters derived from EXAFS Fe K-edge data analysis of C-S-H phases loaded with Fe. Calculated uncertainties are given in parentheses. N = number of neighboring atoms, R = interatomic distance, σ^2 = Debye-Waller factor, ΔE = energy shift, R – factor = residual factor.

Sample	Fe(III) (ppm)	Shell	N	R (Å)	σ^2 (Å^2)	ΔE (eV)	R-factor
C-S-H 1.5	600	Fe-O_1	5.8 (.5)	1.99 (.01)	0.006 (.001)	4.13 (1.1)	0.001
		Fe-Si	4.5 (1.0)	3.57 (.01)	0.008 (.002)		
		Fe-Ca	2.2 (.5)	4.36 (.03)	0.003 (.001)		
		Fe-O_2	14.8 (2.5)	4.45 (.03)	0.005 (.002)		
C-S-H 1.5	12,000	Fe-O_1	5.5 (.6)	2.02 (.01)	0.004 (.001)	4.53 (1.2)	0.002
		Fe-Si	4.8 (.7)	3.62 (.01)	0.008*		
		Fe-Ca	2*	4.35 (.04)	0.003*		
		Fe-O_2	16.1 (2.9)	4.45 (.01)	0.007(.001)		

C-S-H 1.2	900	Fe-O_1	6.7 (1.7)	2.00 (.01)	0.005 (.001)	-2.1 (1.5)	0.005
		Fe-Si	4*	3.56 (.03)	0.008 (.002)		
		Fe-Ca	2*	4.34 (.03)	0.003 (.001)		
		Fe-O_2	15.3 (3.2)	4.43 (.01)	0.005 (.002)		
C-S-H 0.8	600	Fe-O	6*	1.97 (.02)	0.006 (.001)	3.28 (1.5)	0.022
		Fe-Si	4.6 (1.3)	3.15 (.07)	0.005 (.003)		
		Fe-Ca	2.8 (.8)	3.19 (.05)	0.003*		
		Fe-Fe	2*	3.34 (.05)	0.012 (.007)		

*) Fixed parameters.

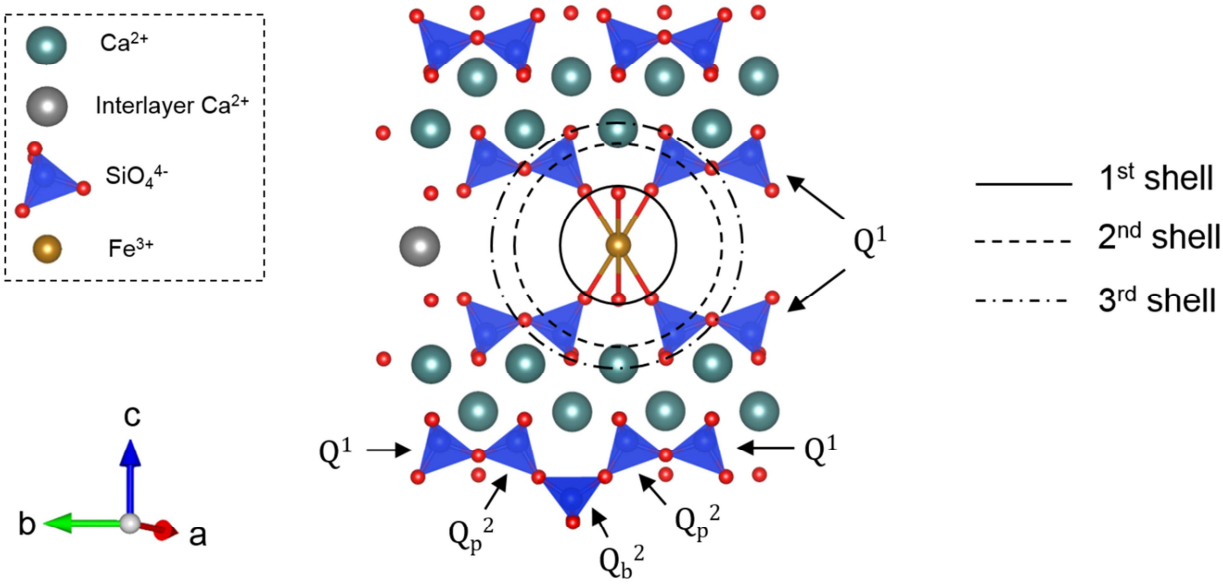

Figure 8: Proposed structural model for the uptake of Fe in the interlayer at high Ca/Si ratio of C-S-H phases. The water molecules in the interlayer are not shown in the model as their number is unknown and depends on drying conditions.

3.3.2.2 Type 1 coordination environment of C-S-H 0.8 at low Fe loading

Several attempts were undertaken to fit the spectra of C-S-H 0.8 loaded with 600 ppm Fe. A multi-shell fit approach based on the structural model of Fe uptake by C-S-H phases as proposed earlier by Labhasetwar et al. (1991) failed. The latter authors reported that Fe can replace Ca in the interlayer space of C-S-H phases with low Ca/Si ratio. Labhasetwar et al. (1991) developed the model solely on the basis of Mössbauer data without providing any supporting evidence.

The 11 Å tobermorite structure proposed by Hamid (1981) was used in the present work as model and an Fe atom was manually inserted close to the bridging site in the interlayer. The Hamid (1981) structure was preferred to the Merlino et al. (2001) structure since it contains less Ca in the interlayer and thus reflects better the studied Ca/Si ratio. In addition, structural models involving two other possible Fe positions in the interlayer, i.e. close to the pair sites and Ca substitution at the bridging site, were tested (see Fig. S5 in SI). They did not improve the fits. As previously mentioned, the ^{29}Si NMR studies suggest that incorporation of Fe in C-S-H phases depends on the Ca/Si ratio and that C-S-H phases with high Ca/Si ratios are more susceptible to Fe incorporation than phases with a low Ca/Si ratio and long silicate chain lengths. The observed variations in centerband linewidth, spinning sideband intensity, signal reduction (I/I_0) and spin-lattice relaxation times support a model at low Ca/Si ratio, where Fe is predominantly bonded to the surface of the C-S-H particles or present as clusters/separate particles respectively. For this purpose, additional multi-shell fits using a Fe-Ca-Si rich mineral as model (e.g. babingtonite - $Ca_2(Fe^{2+},Mn)Fe^{3+}Si_5O_{14}(OH)$ (Araki and Zoltai, 1972)) were performed which resulted in good agreement between the fitted and experimental spectra. As previously described, the first peak represented the backscattering contribution from the nearest oxygen shell. The number of oxygen atoms was fixed to 6 indicating an octahedral geometry in accordance with the weak pre-edge (Fig. 5b). The intensity of the pre-edge was comparable to that in the C-S-H phases with high Ca/Si ratios. Presence of further backscattering was indicated by a broad peak, which was successfully fitted by considering Si, Ca, and Fe atoms. About four neighboring Si atoms were determined at a distance of $R_{Fe\text{-}Si}$ of ~ 3.15 Å ± 0.07 and about three Ca atoms at $R_{Fe\text{-}Ca}$ of ~ 3.19 Å ± 0.05. A third backscattering contribution resulted from two Fe atoms located at a distance of $R_{Fe\text{-}Fe}$ ~ 3.34 Å ± 0.05 but the radial distances were quite close. As a consequence, the spectra could not be accurately fitted if one of these contributions was omitted from the model. The number of Fe as well as the Debye-Waller factor of Ca had to be fixed. The presence of a Fe-Fe contribution, as well as the interatomic distances and the number of neighbors, excludes a possible formation of Fe-Si-Hydrogarnet (Vespa et al., 2015).

The model provided by the multi-shell fit suggests the formation of a secondary phase or clusters presumably on the surface of the C-S-H phase. Fe is octahedrally

coordinated to oxygen atoms in this phase. The other three shells have similar radial distances (in particular the second and third shells) and contain Si, Ca, and Fe, respectively.

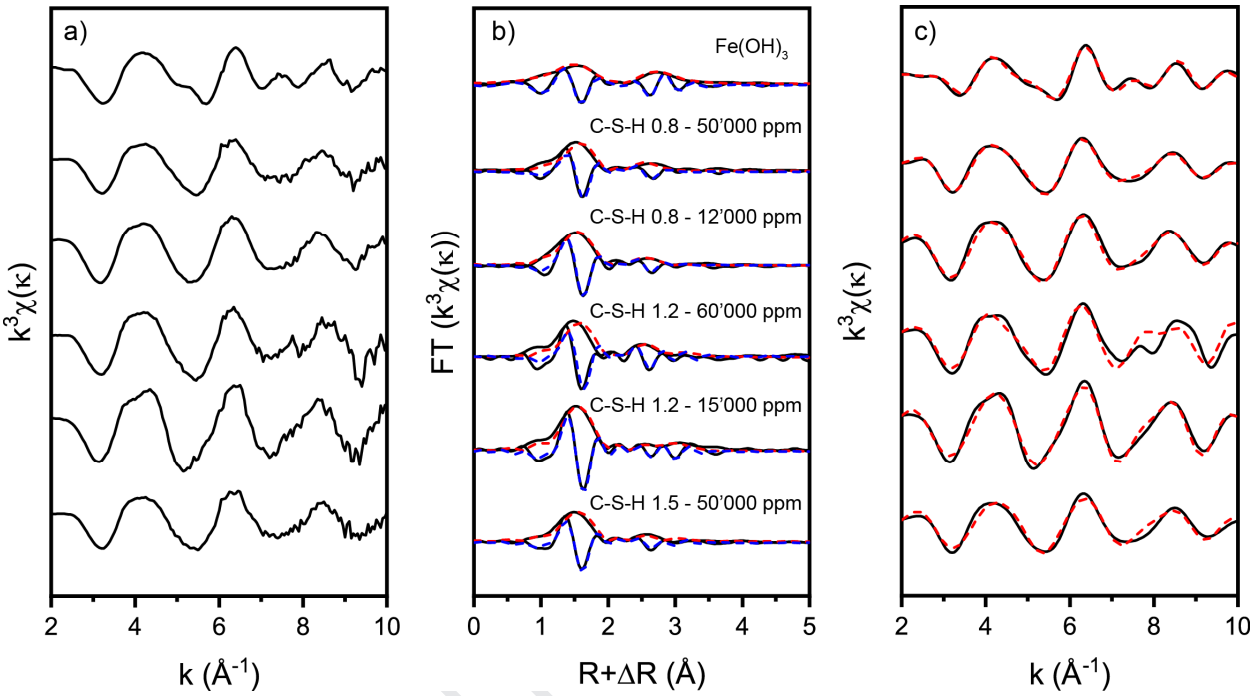

Figure 9: Fe K-edge of $Fe(OH)_3$ and Fe-doped C-S-H phases showing type 2 coordination environment. a) k^3-weighted spectra, b) the corresponding Fourier transform spectra of experimental (black solid line) and fitted (colored dashed lines), c) the k^3-weighted EXAFS function of the Fourier-backtransform spectra obtained from Fig. 9b.

3.3.2.3 Type 2 coordination environment

On the basis of thermodynamic modelling it was expected that the precipitation of microcrystalline or amorphous $Fe(OH)_3$ occurred in C-S-H samples at high Fe loadings (≥ 12,000 ppm). EXAFS spectroscopy was performed on highly Fe-loaded C-S-H samples in order to prove the formation of Fe-hydroxide and decipher the coordination environment of Fe in these conditions. For example, at pH 12.5 and above an aqueous Fe concentration of 10^{-7} mol/L (corresponding to ~ 3000 ppm of sorbed Fe), the C-S-H suspensions was expected to be supersaturated with respect to microcrystalline $Fe(OH)_3$(mc) (Table 1).

In a first stage of data analysis, the structural parameters of the $Fe(OH)_3$ reference were deduced from multi-shell fitting (ΔR = 1 to 5 $Å^{-1}$) by considering a single oxygen shell

(N_O = 5.5, R_{Fe-O} = 1.96 ± 0.03) and two iron shells (N_{Fe1} = 4.0, R_{Fe-Fe1} = 3.03 and N_{Fe2} = 3.9, R_{Fe-Fe2} = 3.42) (Table 5). The fitted structural parameters agree within the experimental uncertainties with parameters reported earlier for an amorphous Fe-hydroxide by Manceau and Drits (1993) (Table 5). All Fe-loaded C-S-H samples showed characteristic backscattering contributions comparable to $Fe(OH)_3$ (Fig. 9). However, Fe bonded to C-S-H phases at the high loadings revealed a slightly lower number of neighboring oxygen atoms compared to $Fe(OH)_3$ (Table 5 and 7). For the Fe-loaded C-S-H samples, N_O varied between 3.6 ± 0.8 and 4.7 ± 1.2, implying a tetrahedral rather than an octahedral coordination sphere. The Fe-O distances agreed with those of $Fe(OH)_3$ within the experimental uncertainty. Furthermore, the low residual indicated good agreement between experimental and modelled spectra. Considering additional backscattering contributions, e.g. by an additional oxygen shell and Ca and Si neighboring atoms, as suggested by Christensen and Christensen (1978) and Szytuła et al. (1968), did not improve the goodness of fit. Therefore, the slightly lower number of neighboring oxygen atoms in C-S-H samples as compared to $Fe(OH)_3$ suggests that the precipitated phase could be a poorly ordered amorphous $Fe(OH)_3$.

The spectra of the C-S-H samples with Ca/Si ratio = 0.8 and loaded with 12,000 ppm and 50,000 ppm Fe revealed the same spectral feature as the C-S-H phases with the higher Ca/Si ratios and data analysis resulted in structural parameters that were consistent with those of the latter C-S-H phases (Table 6). Precipitation of this Fe-rich phase occurred at lower Fe concentration in the C-S-H 0.8 suspension than for the C-S-H 1.2 or 1.5 suspensions in line with the lower solubility of $Fe(OH)_3$ at the lower pH value in the low Ca/Si C-S-H suspension (Table 1).

746

747

748 **Table 7** Structural parameters derived from EXAFS Fe K-edge data analysis of the C-S-H
749 samples showing precipitation. Calculated uncertainties are given in parentheses. N =
750 number of neighboring atoms, R = interatomic distance, σ^2 = Debye-Waller factor, ΔE =
751 energy shift, R – factor = residual factor.

Sample	Fe(III) (ppm)	Shell	N	R (Å)	σ^2 (Å^2)	ΔE (eV)	R-factor
C-S-H 1.5	50,000	Fe-O	3.6 (.8)	2.00 (.02)	0.006 (.004)	4.76 (1.9)	0.001
		Fe-Fe_1	4.0*	3.01 (.05)	0.019 (.008)		
		Fe-Fe_2	3.9*	3.36 (.06)	0.019 (.008)		
C-S-H 1.2	15,000	Fe-O	4.7 (1.2)	2.02 (.02)	0.006 (.004)	3.33 (1.0)	0.002
		Fe-Fe_1	4.7(.9)	3.09(.05)	0.016 (.008)		
		Fe-Fe_2	3.3 (.9)	3.38 (.05)	0.016 (.008)		
C-S-H 1.2	60,000	Fe-O	4.1 (.6)	2.00 (.02)	0.006 (.004)	5.01 (1.3)	0.002
		Fe-Fe_1	4.6 (.6)	3.06 (.04)	0.012 (.005)		
		Fe-Fe_2	3.4 (.7)	3.29 (.01)	0.012 (.004)		
C-S-H 0.8	50,000	Fe-O	4.0 (.5)	2.02 (.02)	0.006 (.003)	5.44 (1.4)	0.008
		Fe-Fe_1	5.2 (1.3)	3.09 (.05)	0.020 (.007)		
		Fe-Fe_2	2.8 (1.3)	3.31 (.09)	0.020 (.007)		
C-S-H 0.8	12,000	Fe-O	4.0 (.6)	1.93 (.02)	0.060 (.040)	4.78 (1.2)	0.001
		Fe-Fe_1	4.8 (.8)	3.01 (.04)	0.021 (.006)		
		Fe-Fe_2	3.2 (.8)	3.29 (.06)	0.021 (.006)		

*) Fixed parameters.

752

753 *3.4 Comparison of Fe(III) and Al(III) uptake by C-S-H phases*

754 A comparison of the sorption data for Fe uptake by C-S-H phases as obtained in this study
755 and those for Al reported earlier by L'Hôpital et al. (2015 and 2016) is shown in Fig. 10a. At
756 the same metal loading, the concentration of Al in solution was about an order of a
757 magnitude higher than that of Fe. Conversely, the Fe loading was about an order of a
758 magnitude higher than that of Al at the same aqueous concentration. The K_d value for Al
759 was estimated to range between 50 and 80 m^3/kg from the data reported in Fig. 10a, while
760 the K_d value for Fe was around 700 m^3/kg (Table 3). This finding shows that Al uptake by C-S-
761 H phases is significantly weaker than that of Fe. It is noteworthy that the difference in
762 sorption intensity is also reflected by the difference in solubility of the Al- and Fe-hydroxides

(Fig. 10b). The solubility diagrams calculated for Fe and Al indicate that the solubility of Al is higher than that of Fe in the studied pH range of 11.5-13.5 (Fig. 10b). Thus, the one order difference in the K_d values corresponds to the almost one order difference in the solubility of gibbsite and $Fe(OH)_3$(am). The maximum uptake of Al by C-S-H, however, is higher than the Fe uptake due to the higher solubility of gibbsite compared to $Fe(OH)_3$.

Aluminium occupies different crystallographic positions in C-A-S-H phases (Renaudin et al., 2009a; L'Hôpital et al., 2016a). At low Ca/Si ratio, Al in tetrahedral coordination replaces Si(IV) at the bridging position of the dreierketten silica chains while at high Ca/Si ratio, Al may also be present in octahedral coordination and competes with other cations (such as Ca) for uptake into the interlayer of the C-S-H phases. In this study, we show that at high Ca/Si ratio, Fe is also octahedrally coordinated in the interlayer of C-S-H phases. Therefore, Fe could compete with Al (and other cations) for uptake into the interlayer. Nevertheless, such possible competitions are expected to occur only at low Fe concentration, where Fe does not precipitate as $Fe(OH)_3$.

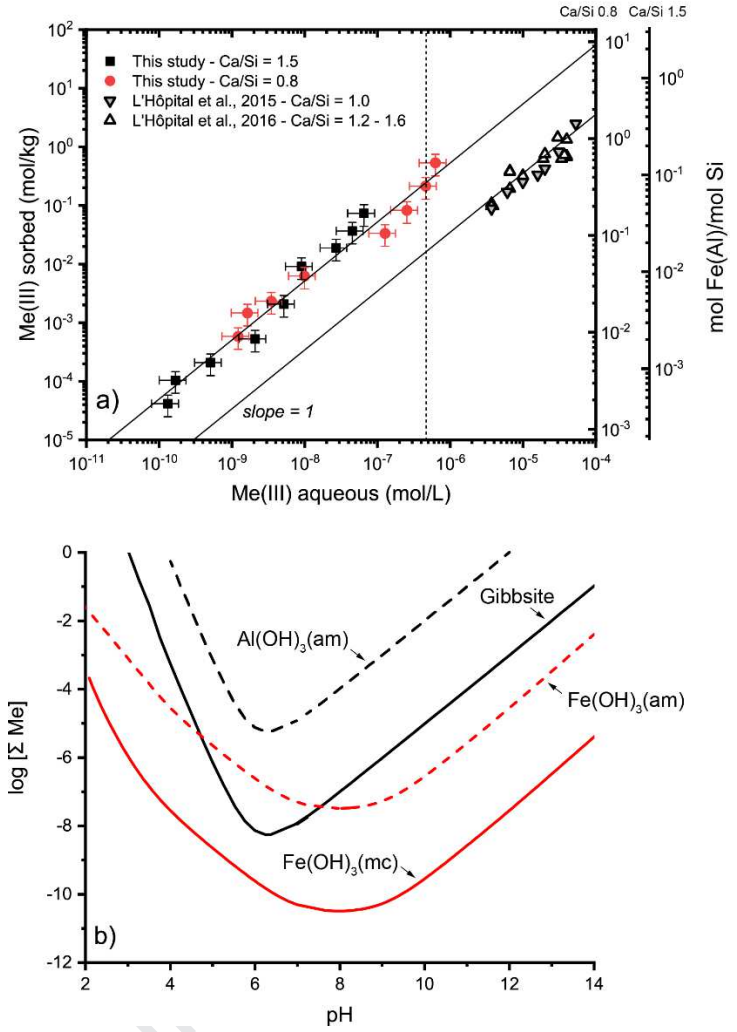

777

778 **Figure 10:** a) Comparison between sorbed Fe and Al in C-S-H phases. The vertical dashed line
779 represents the solubility limit observed by EXAFS spectroscopy. Note the different y-axes for
780 the two Ca/Si ratios. The pH of experiments is as follows: 12.5 in this study, 11.8-11.9 in
781 L'Hôpital et al. (2015), and 12.0-12.6 in L'Hôpital et al. (2016a, b). b) Solubility of amorphous
782 $Al(OH)_3$ (black dashed line), gibbsite (black line), microcrystalline $Fe(OH)_3$ (red line), and
783 amorphous $Fe(OH)_3$ (red dashed line).

784

785 *3.5 Implications for radwaste disposal*

786 This study shows that Fe(III) strongly interacts with C-S-H phases, the most important
787 component of cement paste, and that it is preferentially bonded in the interlayer by
788 coordination to Si tetrahedra of the dreierketten silica chains adjacent to the interlayer

space. In addition, it had been shown previously that Fe(III) can substitute Al in AFt, AFm phases, and siliceous hydrogarnet (Möschner et al., 2008; Möschner et al., 2009; Dilnesa et al., 2011; Dilnesa et al., 2012; Vespa et al., 2015). Hence, the strong interaction of Fe(III) with C-S-H phases and Al-bearing cement phases implies that the mobility of Fe(III) in cement pastes is significantly limited by sorption, for example, at the steel-cement interface where Fe(II,III) oxides and hydroxides are present as products of steel corrosion. The limited solubility of Fe(III) oxides and hydroxides on the one hand, e.g. due to magnetite formed in the course of the anoxic steel corrosion in a repository for radioactive waste, and the strong retardation of Fe(III) by cement phases on the other hand suggests that Fe(III) might preferentially be accumulated in the vicinity of the corrosion front.

The results from this study further show that Fe(III) occupies structural positions in the interlayer that may also accommodate metal cations, in particular actinides. For example, Gaona et al. (2001) identified ~ 8 O atoms, ~ 3 Si atoms and ~ 12 Ca atoms as neighboring atoms for Np(IV)-loaded C-S-H phases. While the number of neighboring Ca atoms seems unrealistically high and may involve also second shell oxygen atoms as demonstrated in this study, Gaona et al. (2011) proposed a structural model for Np(IV) coordination in the interlayer of C-S-H phases similar to that presented for Fe(III) in this study. This finding hence implies that Np(IV) and Fe(III) may occupy the same crystallographic positions in the interlayer which could result in competitive sorption of the two cations.

In summary, Fe(III) either precipitates as Fe(III) hydroxide in cementitious environments, it is incorporated in the crystal structure of cement phases, or it is adsorbed onto their surface, while aqueous concentrations are very low. These processes are not only relevant to assess the fate of Fe(III) in cement systems, but they may also have a competitive effect on other radionuclide uptake.

4 Conclusion

Fe(III) uptake by C-S-H phases occurs within 30 days and the sorption isotherms are linear over a large concentration range of Fe. The K_d value for Fe(III) uptake by C-S-H phases is estimated to be ~700 ± 150 m^3/kg irrespective of the Ca/Si ratios of the C-S-H phases thus indicating very strong bonding of Fe(III). The sorption of Fe on C-S-H phases shows no pH

dependence as indicated from the Fe(III) sorption studies on TiO_2. This finding reveals that other uptake mechanisms than surface complexation may be important. The different effects of pH and Ca on Al(III) and Fe(III) uptake further indicate that Fe(III) is subjected to a different binding mechanism in C-S-H as compared to Al(III).

The NMR and XAS investigations reveal different binding modes of Fe on C-S-H phases with Ca/Si ratio = 1.2 and 1.5 and on C-S-H phase with Ca/Si ratio = 0.8 at low Fe(III) loadings:

- ^{29}Si NMR shows that Fe(III) is possibly located in the interlayer of C-S-H phases at high Ca/Si ratio. The structural parameters deduced from EXAFS spectroscopy support this finding. We propose that Fe(III) is octahedrally coordinated in the interlayer of the C-S-H phases with Ca/Si ratios = 1.2 and 1.5, including direct coordination of Fe(III) to Si tetrahedra of the dreierketten silica chains adjacent to the interlayer space.
- For the C-S-H phase with a low Ca/Si ratio of 0.8 significant Fe(III) uptake by the interlayer can be excluded based on the ^{29}Si NMR data. On the basis of the EXAFS data, Fe(III) is considered to form a separate secondary Ca-Si-rich phase (or clusters) on the surface of C-S-H.

A comparison of the Al(III) and Fe(III) sorption data indicates significantly stronger bonding to Fe(III) by C-S-H phases as compared to Al(III). Fe(III) seems to be preferentially bonded octahedrally in the interlayer space, while Al(III) bonding occurs in IV, V and VI-fold coordination and, further, Al(III) can occupy several crystallographic positions in the C-S-H structure.

The present study indicates that corrosion-induced processes could have an effect on the chemical composition of cement phases at the interface between steel/iron and cementitious materials with implications for radionuclide retention. On the one hand, on the basis of the structural information available from this study on the uptake of Fe(III) by C-S-H phases and the corresponding information available from literature on the uptake of tetravalent actinides (e.g. Np(IV)), sorption competition between actinides and Fe(III) corrosion product is likely to occur. This process could reduce radionuclide retention by the cementitious barrier. On the other hand, formation of Fe(III) corrosion products, which might form due to the limited sorption capacity of cement phases for Fe(III), is likely to have

no detrimental effect on radionuclide retention, or even improve it. Detailed assessments of the two opposite effects have to be based on considerations accounting for the inventories of steel/iron and cementitious materials present in the near field of a repository for radioactive waste.

Supporting Information

Supplementary information section contains four figures and one table. Figures S1 and S2 as well as Table S1 provide additional information in conjunction with the sorption experiments discussed in section 3.1. A comparison between the sorption isotherms and the Fe-doped C-S-H samples prepared for EXAFS spectroscopy and ^{29}Si NMR is shown in Figure S3. Figure S4 Fe K-edge spectra of CaO, SiO_2, and TiO_2. Three verified Fe locations in the C-S-H with Ca/Si = 0.8, which failed as input data to fit the experimental spectra are shown in Figure S4.

Acknowledgments

The authors wish to thank A. Laube (PSI) and J.Tits (PSI) for assistance with the wet chemistry experiments, and F. Winnefeld (Empa) for performing XRD measurements. Thanks are extended to Dr. G. Landrot for assistance during the EXAFS measurements at the Samba beamline and SOLEIL for provision of beamtine. Dr. D. Banerjee is thanked for assistance with the EXAFS measurements at BM26 (Dubble) and the ESRF for the provision of beamtime. Financial support by the Swiss National Science Foundation (grant no. 200021_162342) is kindly acknowledged. G. Geng wants to acknowledge the European Union's Horizon 2020 research and innovation program under the Marie Skłodowska-Curie grant agreement No 701647.

References

881 Allen, A.J., Thomas, J.J., Jennings, H.M., 2007. Composition and density of nanoscale
882 calcium–silicate–hydrate in cement. Nat Mater 6, 311-316.

883 Andersen, M.D., Jakobsen, H.J., Skibsted, J., 2003. Incorporation of aluminum in the calcium
884 silicate hydrate (C-S-H) of hydrated Portland cements: A high-field ^{27}Al and ^{29}Si MAS NMR
885 investigation. lnorg Chem 42, 2280-2287.

886 Ankudinov, A., Ravel, B., Rehr, J., Conradson, S., 1998. Real-space multiple-scattering
887 calculation and interpretation of x-ray-absorption near-edge structure. Phys Rev B 58, 7565-
888 7576.

889 Araki, T., Zoltai, T., 1972. Crystal structure of babingtonite. Z Kristallogr - Cryst Mater 135,
890 355-373.

891 Atkins, M., Bennett, D., Dawes, A., Glasser, F., Kindness, A., Read, D., 1992. A
892 thermodynamic model for blended cements. Cem Concr Res 22, 497-502.

893 Barzgar, S., Lothenbach, B., Tarik, M., Di Giacomo, A., Ludwig, C., 2019. The effect of alkali
894 hydroxide on Al uptake by calcium silicate hydrates (C-S-H). Mater (submitted).

895 Bayliss, P., 1975. Interlayer absorption in C-S-H (I). Cem Concr Res 5, 221−223.

896 Bertolini, L., Elsener, B., Pedeferri, P., Redaelli, E., Polder, R., 2013. Corrosion of steel in
897 concrete. Wiley-Vch, Weinheim; Germany.

898 Brunauer, S., 1972. Further discussion of the helium flow results of R. F. Feldman. Cem
899 Concr Res 2, 749−753.

900 Chapman, N., McCombie, C., 2003. Principles and standards for the disposal of long-lived
901 radioactive wastes. Pergamon, Oxford; UK.

902 Christensen, H., Christensen, A.N., 1978. Hydrogen-bonds of gamma-FeOOH. Acta Chem
903 Scand 32, 87-88.

904 Comarmond, M.J., Payne, T.E., Harrison, J.J., Thiruvoth, S., Wong, H.K., Aughterson, R.D.,
905 Lumpkin, G.R., Müller, K., Foerstendorf, H., 2011. Uranium sorption on various forms of
906 titanium dioxide–influence of surface area, surface charge, and impurities. Environ Sci
907 Technol 45, 5536-5542.

908 Damidot, D., Lothenbach, B., Herfort, D., Glasser, F.P., 2011. Thermodynamics and cement
909 science. Cem Concr Res 41, 679-695.

910 Deschner, F., Winnefeld, F., Lothenbach, B., Seufert, S., Schwesig, P., Dittrich, S., Goetz-
911 Neunhoeffer, F., Neubauer, J., 2012. Hydration of Portland cement with high replacement
912 by siliceous fly ash. Cem Concr Res 42, 1389-1400.

913 Dilnesa, B.Z., Lothenbach, B., Le Saout, G., Renaudin, G., Mesbah, A., Filinchuk, Y., Wichser,
914 A., Wieland, E., 2011. Iron in carbonate containing AFm phases. Cem Concr Res 41, 311-323.

Dilnesa, B.Z., Lothenbach, B., Renaudin, G., Wichser, A., Wieland, E., Jennings, H., 2012. Stability of monosulfate in the presence of iron. J Am Ceram Soc 95, 3305-3316.

Dilnesa, B.Z., Lothenbach, B., Renaudin, G., Wichser, A., Kulik, D., 2014a. Synthesis and characterization of hydrogarnet $Ca_3(Al_xFe_{1-x})_2(SiO_4)_y(OH)_{4(3-y)}$. Cem Concr Res 59, 96-111.

Dilnesa, B.Z., Wieland, E., Lothenbach, G., Dähn, R., Scrivener, K.L., 2014b. Fe-containing phases in hydrated cements. Cem Concr Res. 58, 45-55.

Faucon, P., Le Bescop, P., Adenot, F., Bonville, P., Jacquinot, J., Pineau, F., Felix, B., 1996. Leaching of cement: study of the surface layer. Cem Concr Res 26, 1707-1715.

Gaona, X., Dähn, R., Tits, J., Scheinost, A.C., Wieland, E., 2011. Uptake of Np(IV) by C-S-H phases and cement paste: an EXAFS study. Environ Sci Technol 45, 8765-8771.

Geng, G., Myers, R.J., Qomi, M.J.A., Monteiro, P.J., 2017. Densification of the interlayer spacing governs the nanomechanical properties of calcium-silicate-hydrate. Sci Rep 7, 10986.

Gualtieri, A.F., Passaglia, E., 2006. Rietveld structure refinement of NH_4-exchanged natural chabazite. Eur J Mineral 18, 351-359.

Gutteridge, W.A., Parrott, L.J., 1976. A study of the changes in weight, length and interplanar spacing induced by drying and rewetting synthetic CSH (I). Cem Concr Res 6, 357-366.

Hamid, S., 1981. The crystal structure of the 11 Å natural tobermorite $Ca_{2.25}$ $[Si_3O_{7.5}$ $(OH)_{1.5}]\cdot 1H_2O$. Z Kristallogr - Cryst Mater 154, 189-198.

Harfouche, M., Wieland, E., Dähn, R., Fujita, T., Tits, J., Kunz, D., Tsukamoto, M., 2006. EXAFS study of U(VI) uptake by calcium silicate hydrates. J Colloid Interface Sci 303, 195-204.

Hartman, J.S., Sherriff, B.L., 1991. Silicon-29 MAS NMR of the aluminosilicate mineral kyanite: residual dipolar coupling to aluminum-27 and nonexponential spin-lattice relaxation. J Phys Chem 95, 7575-7579.

Hartman, J.S., Narayanan, A., Rigby, S.S., Sliwinski, D.R., Halden, N.M., Bain, A.D., 2007. Heterogeneities in sol–gel-derived paramagnetics-doped forsterites and willemites—Electron microprobe analysis and stretched-exponential ^{29}Si MAS NMR spin–lattice relaxation studies. Can J Chem 85, 56-65.

Huang, Y.H., Shao, H.B., Wieland, E., Kolditz, O., Kosakowski, G., 2018. A new approach to coupled two-phase reactive transport simulation for long-term degradation of concrete. Constr Build Mater 190, 805-829.

Hummel, W., Berner, U., Curti, E., Pearson, F., Thoenen, T., 2002. Nagra/PSI chemical thermodynamic data base 01/01. Universal Publishers/uPUBLISH.com, USA, also published as Nagra Technical Report NTB 02-16, Nagra, Wettingen, Switzerland, 2002.

Kosakowski, G., Berner, U., 2013. The evolution of clay rock/cement interfaces in a cementitious repository for low-and intermediate level radioactive waste. Phys Chem Earth 64, 65-86.

Kulik, D.A., Wagner, T., Dmytrieva, S.V., Kosakowski, G., Hingerl, F.F., Chudnenko, K.V., Berner, U.R., 2013. GEM-Selektor geochemical modeling package: revised algorithm and GEMS3K numerical kernel for coupled simulation codes. Computat Geosci 17, 1-24.

L'Hôpital, E., Lothenbach, B., Le Saout, G., Kulik, D., Scrivener, K., 2015. Incorporation of aluminium in calcium-silicate-hydrates. Cem Concr Res 75, 91-103.

L'Hôpital, E., Lothenbach, B., Scrivener, K., Kulik, D., 2016a. Alkali uptake in calcium alumina silicate hydrate (CASH). Cem Concr Res 85, 122-136.

L'Hôpital, E., Lothenbach, B., Kulik, D., Scrivener, K., 2016b. Influence of calcium to silica ratio on aluminium uptake in calcium silicate hydrate. Cem Concr Res 85, 111-121.

Labhasetwar, N., Shrivastava, O., Medikov, Y., 1991. Mössbauer study on iron-exchanged calcium silicate hydrate: $Ca_5- xFe_xSi_6O_{18}H_2\cdot nH_2O$. J Solid State Chem 93, 82-87.

Lange, S., Kowalski, P., Pšenička, M., Klinkenberg, M., Rohmen, S., Bosbach, D., Deissmann, G., 2018. Uptake of ^{226}Ra in cementitious systems: A complementary solution chemistry and atomistic simulation study. Appl Geochem 96, 204-216.

Lothenbach, B., Winnefeld, F., 2006. Thermodynamic modelling of the hydration of Portland cement. Cem Concr Res 36, 209-226.

Lothenbach, B., 2010. Thermodynamic equilibrium calculations in cementitious systems. Mater Struct 43, 1413-1433.

Lothenbach, B., Scrivener, K., Hooton, R.D., 2011. Supplementary cementitious materials. Cem Concr Res 41, 1244-1256.

Lothenbach, B., Nonat, A., 2015. Calcium silicate hydrates: Solid and liquid phase composition. Cem Concr Res 78, 57-70.

Lothenbach, B., Kulik, D.A., Matschei, T., Balonis, M., Baquerizo, L., Dilnesa, B., Miron, G.D., Myers, R.J., 2019. Cemdata18: A chemical thermodynamic database for hydrated Portland cements and alkali-activated materials. Cem Concr Res 115, 472-506.

Manceau, A., Drits, V., 1993. Local structure of ferrihydrite and feroxyhite by EXAFS spectroscopy. Clays Clay Miner 28, 165-184.

Mancini, A., Wieland, E., Geng, G., Dähn, R., Wehrli, B., Lothenbach, B., 2019. Fe(II) interaction with cement phases. Cem Concr Res (in prep.).

Mandaliev, P., Wieland, E., Dähn, R., Tits, J., Churakov, S., Zaharko, O., 2010a. Mechanisms of Nd(III) uptake by 11 Å tobermorite and xonotlite. Appl Geochem 25, 763-777.

Mandaliev, P., Dähn, R., Tits, J., Wehrli, B., Wieland, E., 2010b. EXAFS study of Nd (III) uptake by amorphous calcium silicate hydrates (C–S–H). J Colloid Interface Sci 342, 1-7.

Markley, J.L., Horsley, W.J., Klein, M.P., 1971. Spin-lattice relaxation measurements in slowly relaxing complex spectra. J Phys Chem 55, 3604-3605.

Merlino, S., Bonaccorsi, E., Armbruster, T., 1999. Tobermorites: Their real structure and order-disorder (OD) character. Am Mineral 84, 1613-1621.

Merlino, S., Bonaccorsi, E., Armbruster, T., 2001. The real structure of tobermorite 11Å: normal and anomalous forms, OD character and polytypic modifications. Eur J Mineral 13, 577-590.

Möschner, G., Lothenbach, B., Rose, J., Ulrich, A., Figi, R., Kretzschmar, R., 2008. Solubility of Fe–ettringite ($Ca_6[Fe(OH)_6]_2(SO_4)_3{\cdot}26H_2O$). Geochim Cosmochim Acta 72, 1-18.

Möschner, G., Lothenbach, B., Winnefeld, F., Ulrich, A., Figi, R., Kretzschmar, R., 2009. Solid solution between Al-ettringite and Fe-ettringite ($Ca_6[Al_{1-x}Fe_x(OH)_6]_2(SO_4)_3{\cdot}26H_2O$). Cem Concr Res 39, 482-489.

Myers, R.J., L'Hôpital, E., Provis, J.L., Lothenbach, B., 2015. Effect of temperature and aluminium on calcium (alumino) silicate hydrate chemistry under equilibrium conditions. Cem Concr Res 68, 83-93.

Olmeda, J., Missana, T., Grandia, F., Grivé, M., García-Gutiérrez, M., Mingarro, M., Alonso, U., Colàs, E., Henocq, P., Munier, I., Robinet, J.C., 2019. Radium retention by blended cement pastes and pure phases (C-S-H and C-A-S-H gels): Experimental assessment and modelling exercises. Appl Geochem 105, 45-54.

Pointeau, I., Piriou, B., Fedoroff, M., Barthes, M.-G., Marmier, N., Fromage, F., 2001. Sorption mechanisms of Eu^{3+} on CSH phases of hydrated cements. J Colloid Interface Sci 236, 252-259.

Pokrovski, G.S., Schott, J., Farges, F., Hazemann, J.-L., 2003. Iron(III)-silica interactions in aqueous solution: Insights from X-ray absorption fine structure spectroscopy. Geochim Cosmochim Acta 67, 3559-3573.

Poulsen, S.L., Kocaba, V., Le Saoût, G., Jakobsen, H.J., Scrivener, K.L., Skibsted, J., 2009. Improved quantification of alite and belite in anhydrous Portland cements by ^{29}Si MAS NMR: effects of paramagnetic ions. Solid State Nucl Magn Reson 36, 32-44.

Ravel, B., Newville, M., 2005. ATHENA, ARTEMIS, HEPHAESTUS: data analysis for X-ray absorption spectroscopy using IFEFFIT. J Synchrotron Radiat 12, 537-541.

Rehr, J., Mustre de Leon, J., Zabinsky, S., Albers, R., 1991. Theoretical X-ray absorption fine structure standards. J Am Chem Soc 113, 5135-5140.

Renaudin, G., Russias, J., Leroux, F., Cau-dit-Coumes, C., Frizon, F., 2009a. Structural characterization of C–S–H and C–A–S–H samples—Part II: Local environment investigated by spectroscopic analyses. J Solid State Chem 182, 3320-3329.

Renaudin, G., Russias, J., Leroux, F., Frizon, F., Cau-dit-Coumes, C., 2009b. Structural characterization of C-S-H and C-A-S-H samples—part I: long-range order investigated by Rietveld analyses. J Solid State Chem 182, 3312-3319.

Richardson, I., 2004. Tobermorite/jennite-and tobermorite/calcium hydroxide-based models for the structure of CSH: applicability to hardened pastes of tricalcium silicate, β-dicalcium silicate, Portland cement, and blends of Portland cement with blast-furnace slag, metakaolin, or silica fume. Cem Concr Res 34, 1733-1777.

Richardson, I.G., 2014. Model structures for C-(A)-S-H (I). Acta Crystallogr Sect B: Struct Sci 70, 903-923.

Richardson, I.G., Brough, A.R., Brydson, R., Groves, G.W., Dobson, C.M., 1993. Location of aluminum in substituted calcium silicate hydrate (C-S-H) gels as determined by ^{29}Si and ^{27}Al NMR and EELS. J Am Ceram Soc 76, 2285-2288.

Roosz, C., Gaboreau, S., Grangeon, S., Prêt, D., Montouillout, V., Maubec, N., Henocq, P., 2016. Distribution of water in synthetic calcium silicate hydrates. Langmuir 32, 6794-6805.

Schlegel, M.L., Pointeau, I., Coreau, N., Reiller, P., 2004. Mechanism of europium retention by calcium silicate hydrates: an EXAFS study. Environ Sci Technol 38, 4423-4431.

Schmidt, J., Vogelsberger, W., 2009. Aqueous long-term solubility of titania nanoparticles and titanium(IV) hydrolysis in a sodium chloride system studied by adsorptive stripping voltammetry. J Solution Chem 38, 1267-1282.

Sipos, P., Zeller, D., Kuzmann, E., Vértes, A., Homonnay, Z., Walczak, M., Canton, S.E., 2008. The structure of Fe(III) ions in strongly alkaline aqueous solutions from EXAFS and Mössbauer spectroscopy. Dalton Trans, 5603-5611.

Skibsted, J., Jakobsen, H.J., Hall, C., 1995. Quantification of calcium silicate phases in Portland cements by 29 Si MAS NMR spectroscopy. J Chem Soc, Faraday Trans 91, 4423-4430.

Smith, R.H., Bayliss, P., 1972. Interlayer desorption of C-S-H (1). Cem Concr Res 2, 643−646.

Stefanoni, M., Zhang, Z., Angst, U.M., Elsener, B., 2018. The kinetic competition between transport and oxidation of ferrous ions governs precipitation of corrosion products in carbonated concrete. RILEM Tech Lett 3, 8-16.

Suda, Y., Saeki, T., Saito, T., 2015. Relation between chemical composition and physical properties of CSH generated from cementitious materials. J Adv Concr Technol 13, 275-290.

Szytuła, A., Burewicz, A., Dimitrijević, Ž., Kraśnicki, S., Rżany, H., Todorović, J., Wanic, A., Wolski, W., 1968. Neutron diffraction studies of α-FeOOH. Phys Status Solidi 26, 429-434.

1054 Taylor, H., 1997. Cement chemistry. Thomas Telford, London, UK.

1055 Taylor, R., Richardson, I., Brydson, R., 2010. Composition and microstructure of 20-year-old
1056 ordinary Portland cement–ground granulated blast-furnace slag blends containing 0 to 100%
1057 slag. Cem Concr Res 40, 971-983.

1058 Thoenen, T., Hummel, W., Berner, U., Curti, E., 2014. The PSI/Nagra chemical
1059 thermodynamic database 12/07. PSI Report Nr. 14-04, Paul Scherrer Institut, Villigen PSI,
1060 Switzerland.

1061 Tits, J., Gaona, X., Laube, A., Wieland, E., 2014. Influence of the redox state on the
1062 neptunium sorption under alkaline conditions: Batch sorption studies on titanium dioxide
1063 and calcium silicate hydrates. Radiochim Acta 102, 385-400.

1064 Tits, J., Geipel, G., Macé, N., Eilzer, M., Wieland, E., 2011. Determination of uranium(VI)
1065 sorbed species in calcium silicate hydrate phases: A laser-induced luminescence
1066 spectroscopy and batch sorption study. J Colloid Interface Sci 359, 248-256.

1067 Tits, J., Wieland, E., Müller, C., Landesman, C., Bradbury, M., 2006a. Strontium binding by
1068 calcium silicate hydrates. J Colloid Interface Sci 300, 78-87.

1069 Tits, J., Iijima, K., Wieland, E., Kamei, G., 2006b. The uptake of radium by calcium silicate
1070 hydrates and hardened cement paste. Radiochim Acta 94, 637-643.

1071 Tits, J., Wieland, E., Bradbury, M.H., Eckert, P., Schaible, A., 2002. The uptake of Eu(III) and
1072 Th(IV) by calcite under hyperalkaline conditions. PSI Report Nr. 02-03, Paul Scherrer Institut,
1073 Villigen PSI, Switzerland, and Nagra Technical Report NTB 02-08, Nagra, Wettingen,
1074 Switzerland.

1075 Tse, D., Hartmann, S., 1968. Nuclear spin-lattice relaxation via paramagnetic centers without
1076 spin diffusion. Phys Rev Lett 21, 511-514.

1077 Vespa, M., Wieland, E., Dähn, R., Lothenbach, B., 2015. Identification of the
1078 Thermodynamically Stable Fe-Containing Phase in Aged Cement Pastes. J Am Ceram Soc 98,
1079 2286-2294.

1080 Wang, X., Zhu, M., Koopal, L.K., Li, W., Xu, W., Liu, F., Zhang, J., Liu, Q., Feng, X., Sparks, D.L.,
1081 2016. Effects of crystallite size on the structure and magnetism of ferrihydrite. Environ Sci
1082 Nano 3, 190-202.

1083 Wilke, M., Farges, F., Petit, P.-E., Brown Jr, G.E., Martin, F., 2001. Oxidation state and
1084 coordination of Fe in minerals: An Fe K-XANES spectroscopic study. Am Mineral 86, 714-730.

1085 Ziegler, F., Scheidegger, A.M., Johnson, C.A., Dähn, R., Wieland, E., 2001. Sorption
1086 mechanisms of zinc to calcium silicate hydrate: X-ray absorption fine structure (XAFS)
1087 investigation. Environ Sci Technol 35, 1550-1555.

1088

Highlights

- Fe(III) is strongly sorbed into the C-S-H structure
- At high Ca/Si ratio of C-S-H, Fe(III) is taken up in the interlayer with an octahedral geometry
- At low Ca/Si ratio of C-S-H, Fe(III) is not bound in the interlayer but rather forms a Fe-rich phase on the surface of C-S-H
- Fe(III) uptake by C-S-H is stronger than that of Al(III)

Declaration of interests

☒ The authors declare that they have no known competing financial interests or personal relationships that could have appeared to influence the work reported in this paper.

☐The authors declare the following financial interests/personal relationships which may be considered as potential competing interests: